LETTER

doi:10.1038/nature19101

Sea-ice transport driving Southern Ocean salinity and its recent trends

F. Alexander Haumann[1,2], Nicolas Gruber[1,2], Matthias Münnich[1], Ivy Frenger[1,3] & Stefan Kern[4]

Recent salinity changes in the Southern Ocean[1–7] are among the most prominent signals of climate change in the global ocean, yet their underlying causes have not been firmly established[1,3,4,6]. Here we propose that trends in the northward transport of Antarctic sea ice are a major contributor to these changes. Using satellite observations supplemented by sea-ice reconstructions, we estimate that wind-driven[8,9] northward freshwater transport by sea ice increased by 20 ± 10 per cent between 1982 and 2008. The strongest and most robust increase occurred in the Pacific sector, coinciding with the largest observed salinity changes[4,5]. We estimate that the additional freshwater for the entire northern sea-ice edge entails a freshening rate of −0.02 ± 0.01 grams per kilogram per decade in the surface and intermediate waters of the open ocean, similar to the observed freshening[1–5]. The enhanced rejection of salt near the coast of Antarctica associated with stronger sea-ice export counteracts the freshening of both continental shelf[2,10,11] and newly formed bottom waters[6] due to increases in glacial meltwater[12]. Although the data sources underlying our results have substantial uncertainties, regional analyses[13] and independent data from an atmospheric reanalysis support our conclusions. Our finding that northward sea-ice freshwater transport is also a key determinant of the mean salinity distribution in the Southern Ocean further underpins the importance of the sea-ice-induced freshwater flux. Through its influence on the density structure of the ocean, this process has critical consequences for the global climate by affecting the exchange of heat, carbon and nutrients between the deep ocean and surface waters[14–17].

Observations of salinity in the Southern Ocean over the past few decades have revealed a substantial widespread freshening in the surface waters of both coastal[10,18] and open ocean regions[2,5], as well as in the water masses formed from them[1,3,4,6]. In particular, the Antarctic Intermediate Water (AAIW) and Subantarctic Mode Water (SAMW) freshened at a rate between −0.01 g kg^{-1} and −0.03 g kg^{-1} per decade during the second half of the twentieth century[1,3,4]. In the Pacific and Indian Ocean sectors, continental shelf waters and the Antarctic Bottom Water (AABW) also freshened substantially[2,6,10], while in the Atlantic this freshening was smaller[6,18]. These salinity changes have been attributed to increased surface freshwater fluxes that stem

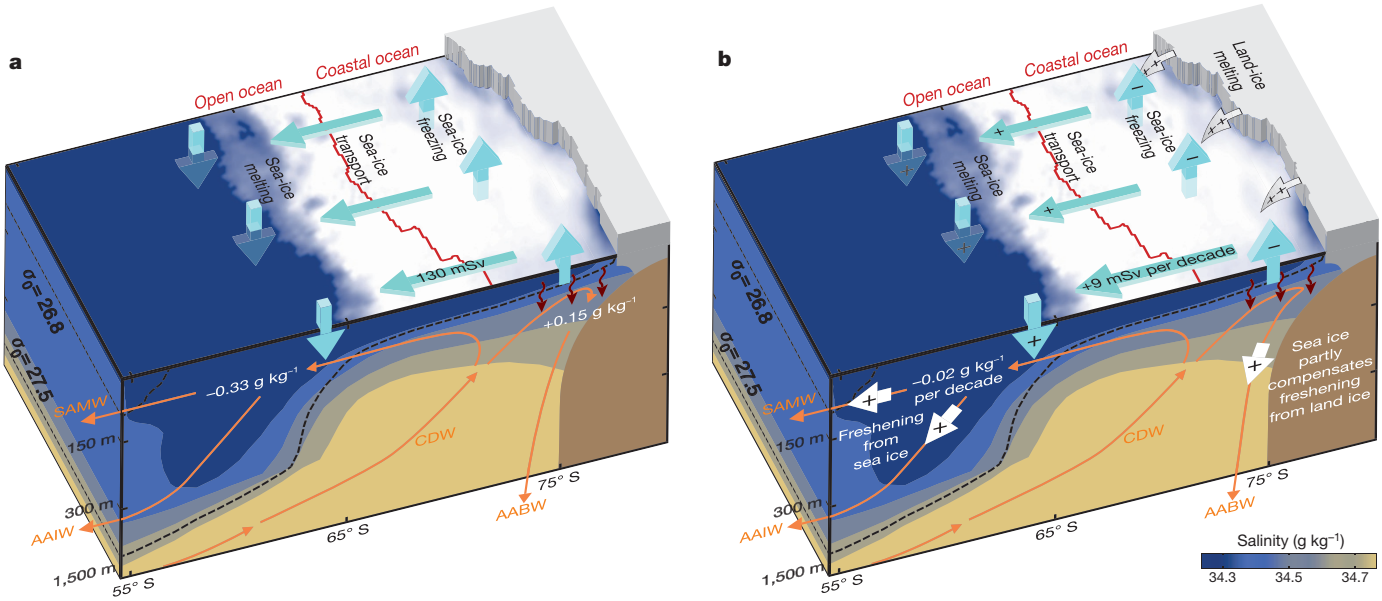

Figure 1 | Effect of northward sea-ice freshwater transport on Southern Ocean salinity. a, **b**, Schematic cross-sections illustrating the effect of northward sea-ice freshwater transport (blue arrows) on mean ocean salinity (**a**) and on the trends over the period 1982 through 2008 (**b**) (see Methods). The red line separates the open and coastal ocean regions. The increasing sea-ice transport freshened the open ocean and, by leaving the salt behind in the coastal region (red curved arrows), compensated for part of the freshening by enhanced glacial meltwater input (grey arrows). White arrows in **b** indicate the freshening effect from both sea ice and land ice. Positive fluxes are defined downwards or northwards. The orange arrows indicate ocean circulation. The background shows the mean salinity (colour scale) and density (dashed black lines) separating Circumpolar Deep Water (CDW) from Antarctic Intermediate Water (AAIW) and Subantarctic Mode Water (SAMW). AABW, Antarctic Bottom Water.

[1]Environmental Physics, Institute of Biogeochemistry and Pollutant Dynamics, ETH Zürich, Universitätstrasse 16, 8092 Zürich, Switzerland. [2]Center for Climate Systems Modeling, ETH Zürich, Universitätstrasse 16, 8092 Zürich, Switzerland. [3]Biogeochemical Modelling, GEOMAR Helmholtz Centre for Ocean Research Kiel, Düsternbrooker Weg 20, 24105 Kiel, Germany. [4]Integrated Climate Data Center (ICDC), Center for Earth System Research and Sustainability, University of Hamburg, Hamburg, Germany.

either from enhanced Antarctic glacial melt[2,6,10–12] or from increased atmospheric freshwater fluxes, as a result of an excess of precipitation over evaporation[1,5]. Glacial meltwater[12] is the most likely cause of the freshened coastal waters in the Amundsen and Ross seas[2,10,11], but the freshening signal in the AABW, which is formed in this region, is much smaller than expected[6]. In contrast, the recent freshening of the AAIW seems to be much larger than can be explained by the simulated increases in the atmospheric freshwater flux by global climate models in the open Southern Ocean[1,4].

Changes in northward sea-ice transport could possibly contribute to the widespread salinity changes in the Southern Ocean[8]. This process acts as a lateral conveyor of freshwater by extracting freshwater from the coastal regions around Antarctica where the sea ice forms and releasing it at the northern edge of the sea ice where the sea ice melts[19–21] (Fig. 1a). Despite substantial wind-driven changes in sea-ice drift over the past few decades[8,9], this contribution has not yet been quantified. Here we suggest that surface freshwater fluxes induced by stronger northward sea-ice transport are a major cause of the observed salinity changes in recent decades; this is corroborated by our finding that the transport process plays a key role in the long-term mean salinity distribution in the Southern Ocean.

Our conclusions are based on basin-scale estimates of annual net sea-ice–ocean freshwater fluxes and the annual northward transport of freshwater by sea ice over the period 1982–2008. Further evidence is provided by our assessment of atmospheric reanalysis data[22] and the results from a regional study[13]. We derived the sea-ice-related freshwater fluxes by combining sea-ice concentration, drift and thickness data and by using a mass balance approach to determine the volume divergence and local change in sea ice (Methods). The sea-ice concentration is derived from satellite observations[23] (Extended Data Fig. 1) and its thickness from a combination of satellite data[24] and a model-based sea-ice reconstruction that assimilates satellite data[25] (Extended Data Fig. 2). The sea-ice volume divergence was computed from satellite-based sea-ice drift vectors[26] (Extended Data Figs 3, 4) and sea-ice volume. From the resulting sea-ice volume budget, we estimated the freshwater equivalents of local annual sea-ice–ocean fluxes due to freezing and melting and annual lateral sea-ice transport (Methods).

Uncertainties in these derived freshwater flux products are substantial (Methods). A major challenge arises from the need to combine sea-ice drift estimates from different satellites to estimate the trends. We addressed potential inhomogeneities and biases by vigorous data quality control, implementing several corrections and considering different time periods (Methods). A second challenge is associated with the relatively limited number of observations of sea-ice thickness. These uncertainties plus the observationally constrained range of the other input quantities were incorporated into our error estimates of the final freshwater flux product (Extended Data Tables 1, 2). In the Atlantic sector, uncertainties associated with the mean sea-ice thickness distribution dominate the uncertainty, while in the Pacific sector uncertainties are mostly caused by uncertainties in sea-ice drift.

Our analysis reveals large trends in the meridional sea-ice freshwater transport in the Southern Ocean between 1982 and 2008 (Figs 1b and 2c) that affect the regional sea-ice–ocean freshwater fluxes (Fig. 2d). The annual northward sea-ice freshwater transport of 130 ± 30 mSv ($1\ \text{mSv} = 1{,}000\ \text{m}^3\ \text{s}^{-1} \approx 31.6\ \text{Gt yr}^{-1}$; Fig. 2a; Extended Data Table 1) from the coastal region to the open ocean strengthened by $+9 \pm 5$ mSv per decade (Extended Data Table 2). Here, the coastal ocean refers to the region between the Antarctic coast and the zero sea-ice–ocean freshwater flux line and the open ocean is the region between the zero sea-ice–ocean freshwater flux line and the sea-ice edge (Fig. 2b). The increased northward transport caused, on average, an additional extraction of freshwater from the coastal ocean of $-40 \pm 20\ \text{mm yr}^{-1}$ per decade and an increased addition to the open ocean region of $+20 \pm 10\ \text{mm yr}^{-1}$ per decade.

The overall intensification occurred primarily in the Pacific sector where we find a vigorous northward freshwater transport trend of

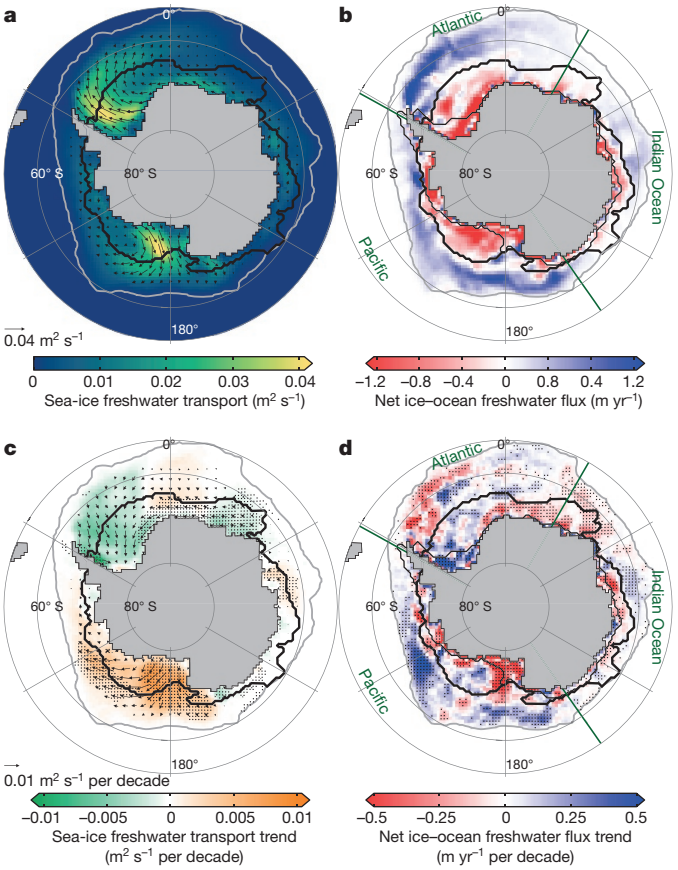

Figure 2 | Mean state and trends of net annual freshwater fluxes associated with sea ice over the period 1982–2008. a, Mean sea-ice-induced freshwater transport. **b**, Mean net sea-ice–ocean freshwater flux. **c**, **d**, Linear trends of northward sea-ice freshwater transport (**c**) and net sea-ice–ocean freshwater flux from freezing and melting (**d**). Stippled areas are significant at the 90% confidence level using Student's *t*-test (see Methods). The arrows show the mean (**a**) and trend (**c**) of the annual transport vectors. The thick black lines indicate the zero sea-ice–ocean freshwater flux line that divides the coastal from the open ocean regions, the thin black lines show the continental shelf (1,000 m isobath). The grey lines represent the edge of the sea ice (1% sea-ice concentration) and the green lines show the boundaries of the ocean basins labelled.

$+14 \pm 5$ mSv per decade. The trends in this sector are the most robust (Extended Data Table 3). Over the whole period, this change in the Pacific sector corresponds to an increase of about 30% with respect to the climatological mean in the entire Southern Ocean (Extended Data Table 1). The largest trends occurred locally in the high-latitude Ross Sea (Fig. 2c, d), where our estimated trends agree well with a previous study[13] (Methods). The increase in the Pacific sector is partly compensated for by small decreases in the Atlantic and Indian ocean sectors. We reach similar conclusions when we consider only the satellite data from 1992 to 2004, that is, the period when they are least affected by potential inhomogeneities (Extended Data Table 3).

The reason for the observed northward sea-ice freshwater transport and its recent trends is the strong southerly winds over the Ross and Weddell seas, which persistently blow cold air from Antarctica over the ocean, pushing sea ice northwards[9]. The winds over the Ross Sea considerably strengthened in recent decades, possibly owing to a combination of natural variability, changes in greenhouse gas concentrations and stratospheric ozone depletion[9]. These changes in the southerly winds induced regional changes in northward sea-ice drift[8,9], which are responsible for the sea-ice freshwater transport trends (Methods). This relation between the atmospheric circulation and sea-ice drift changes enabled us to independently estimate the sea-ice

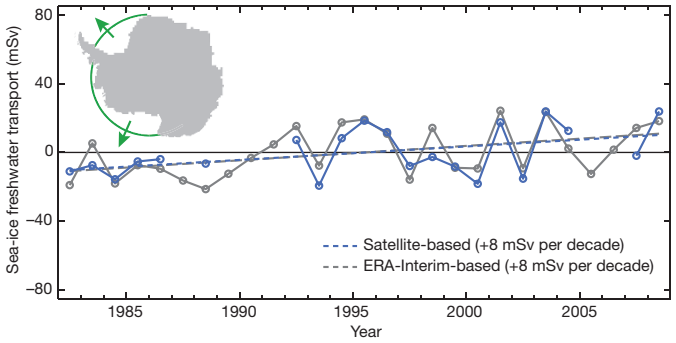

Figure 3 | Time series of annual northward sea-ice freshwater transport anomalies across latitude bands. The underlying sea-ice drift data are based on two independent data sources: the corrected NSIDC satellite data (blue) and zonal sea-level pressure gradients from ERA-Interim data (grey; see Methods). The dashed lines show the respective linear regressions. The map (inset) shows the latitude bands in the Atlantic (69.5° S) and Pacific (71° S) sectors.

drift anomalies using sea-surface pressure gradients along latitude bands from atmospheric reanalysis data[22] (Methods). Comparing the resulting northward sea-ice transport anomalies to the satellite-based estimates across the same latitude bands results in a similar overall trend (Fig. 3). Thus, this alternative approach not only corroborates our estimated long-term trend, but also suggests that any remaining inhomogeneities in the sea-ice drift data that are due to changes in the satellite instruments are comparably small after applying multiple corrections (Methods).

To assess how the changing sea-ice–ocean freshwater flux (Fig. 2d) affected the salinity in the Southern Ocean we assumed that the additional freshwater in the open ocean region entered the AAIW and the SAMW formed from upwelling Circumpolar Deep Waters (CDW)[27,28] (Methods). We find that our freshwater flux trends imply a freshening at a rate of -0.02 ± 0.01 g kg^{-1} per decade in the surface waters that are transported northwards and form the AAIW and SAMW (Fig. 1b). Thus, the sea-ice freshwater flux trend could account for a substantial fraction of the observed long-term freshening in these water masses[1,3,4]. The strong sea-ice–ocean freshwater flux trends in the Pacific sector (Fig. 2d) spatially coincide with the region of largest observed surface freshening[2,5] (Extended Data Fig. 7) and can explain also the stronger freshening of the Pacific AAIW compared with that of the Atlantic[1,4]. A more quantitative attribution of the observed salinity trends to the freshwater transport trends is beyond the scope of our study because the observed freshening trends stem from different time periods, and have strong regional variations and large uncertainties themselves[1,3,4]. However, our data show that changes in northward sea-ice freshwater transport induce salinity changes of comparable magnitude to the observed trends.

Our estimates in coastal regions (Fig. 2d) also help to explain the observed salinity changes in the AABW[6], which is sourced from this region. Additional glacial meltwater from West Antarctica[12] strongly freshened the continental shelf in the Ross and Amundsen seas over recent decades[2,10,11] (Fig. 1b). However, the observed freshening in Pacific and Indian Ocean AABW was found to be much smaller than expected from this additional glacial meltwater[6]. Our data suggests that the freshening induced by the increasing glacial meltwater is substantially reduced by a salinification from an increased sea-ice to ocean salt flux over the continental shelf in the Pacific sector. This salt flux trend corresponds to a freshwater equivalent of -10 ± 3 mSv per decade, resulting from increasing northward sea-ice export from this region of enhanced sea-ice formation (Fig. 2c, d). In contrast, over the continental shelf in the Atlantic sector our data suggest a decreasing sea-ice to ocean salt flux, corresponding to a freshwater equivalent of $+6 \pm 3$ mSv per decade, which may have contributed to the observed freshening of the newly formed Atlantic AABW[6] and the north-western continental shelf waters[18].

The large contribution of the trends in sea-ice freshwater transport to recent salinity changes in the Southern Ocean is in line with the dominant role that sea ice plays in the surface freshwater budget in the seasonal sea-ice zone[29] and in the global overturning circulation[19–21,27] in the mean state. The freshwater equivalent of the total Southern Ocean sea-ice melting flux (Fig. 4a) is as large as 460 ± 100 mSv (Extended Data Table 1). On an annual basis, the vast majority of this melting flux is supplied by the freezing of seawater of -410 ± 110 mSv, with the remaining flux arising from snow-ice formation[30] (Methods; Fig. 4b). Most of the sea ice is produced in the coastal region (-320 ± 70 mSv), but only about 60% of the sea ice also melts there. The rest, that is, 130 ± 30 mSv, is exported to the open ocean (Fig. 4c). These mean estimates agree well with an independent parallel study[27], which is based on the assimilation of Southern Ocean salinity and temperature observations (Methods).

The process of northward freshwater transport by sea ice effectively removes freshwater from waters that enter the lower oceanic overturning cell, in particular the AABW, and adds it to the upper circulation cell, especially the AAIW (Fig. 1a). Through this process, the salinity difference between these two water masses, and thus the meridional and vertical salinity gradients, increase. In a steady state, the northward sea-ice freshwater transport of 130 ± 30 mSv implies a salinity modification of $+0.15 \pm 0.06$ g kg^{-1} and -0.33 ± 0.09 g kg^{-1}

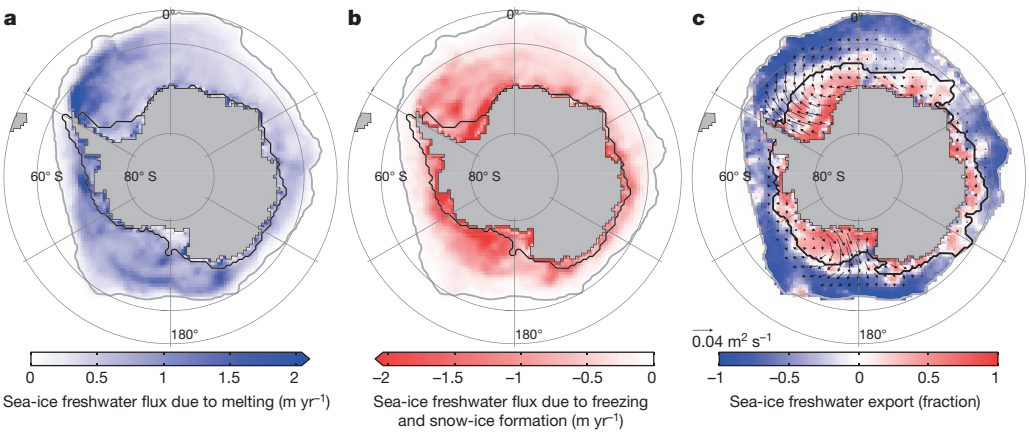

Figure 4 | Mean annual sea-ice-related freshwater fluxes associated with melting, freezing and transport over the period 1982–2008. a, Sea-ice–ocean freshwater flux due to melting. **b**, Freshwater flux associated with freezing and the formation of snow ice. **c**, Fraction of freshwater exported relative to local freezing flux (red) and imported relative to the local melting flux (blue) due to sea-ice induced freshwater transport (arrows). Black and grey lines as in Fig. 2.

in waters that are entering the lower and upper cell, respectively (Methods). The latter suggests that sea-ice freshwater transport accounts for the majority of the salinity difference between the upwelling CDW and the exiting AAIW. We estimated that the salinification from sea ice in waters entering the lower circulation cell is compensated by glacial meltwater and excess precipitation over evaporation in this region in about equal parts, agreeing with the very small salinity difference between the CDW and AABW (Methods).

Because salinity dominates the density structure in polar oceans[14], our findings imply that sea-ice transport is a key factor for the vertical and meridional density gradients in the Southern Ocean and their recent changes (Fig. 1). This interpretation is consistent with the observation that large areas of the upper Southern Ocean not only freshened but also stratified in recent decades[7]. Increased stratification potentially hampers the mixing of deeper, warmer and carbon-rich waters into the surface layer and thus could increase the net uptake of CO_2[14,16,17]. Consequently, our results suggest that Antarctic sea-ice freshwater transport, through its influence on ocean stratification and the carbon cycle, is more important for changes in global climate[14,15] than has been appreciated so far. This implication of our findings for the climate system stresses the need to better constrain spatial patterns as well as temporal variations in sea-ice–ocean fluxes by reducing the uncertainties in the observations of drift, thickness and snow cover of Antarctic sea ice.

Online Content Methods, along with any additional Extended Data display items and Source Data, are available in the online version of the paper; references unique to these sections appear only in the online paper.

Received 9 November 2015; accepted 8 July 2016.

1. Wong, A. P. S., Bindoff, N. L. & Church, J. A. Large-scale freshening of intermediate waters in the Pacific and Indian oceans. *Nature* **400,** 440–443 (1999).
2. Jacobs, S. S., Giulivi, C. F. & Mele, P. A. Freshening of the Ross Sea during the late 20th century. *Science* **297,** 386–389 (2002).
3. Böning, C. W., Dispert, A., Visbeck, M., Rintoul, S. R. & Schwarzkopf, F. U. The response of the Antarctic Circumpolar Current to recent climate change. *Nat. Geosci.* **1,** 864–869 (2008).
4. Helm, K. P., Bindoff, N. L. & Church, J. A. Changes in the global hydrological-cycle inferred from ocean salinity. *Geophys. Res. Lett.* **37,** L18701 (2010).
5. Durack, P. J., Wijffels, S. E. & Matear, R. J. Ocean salinities reveal strong global water cycle intensification during 1950 to 2000. *Science* **336,** 455–458 (2012).
6. Purkey, S. G. & Johnson, G. C. Antarctic Bottom Water warming and freshening: contributions to sea level rise, ocean freshwater budgets, and global heat gain. *J. Clim.* **26,** 6105–6122 (2013).
7. de Lavergne, C., Palter, J. B., Galbraith, E. D., Bernardello, R. & Marinov, I. Cessation of deep convection in the open Southern Ocean under anthropogenic climate change. *Nat. Clim. Change* **4,** 278–282 (2014).
8. Holland, P. R. & Kwok, R. Wind-driven trends in Antarctic sea-ice drift. *Nat. Geosci.* **5,** 872–875 (2012).
9. Haumann, F. A., Notz, D. & Schmidt, H. Anthropogenic influence on recent circulation-driven Antarctic sea ice changes. *Geophys. Res. Lett.* **41,** 8429–8437 (2014).
10. Jacobs, S. S. & Giulivi, C. F. Large multidecadal salinity trends near the Pacific–Antarctic continental margin. *J. Clim.* **23,** 4508–4524 (2010).
11. Nakayama, Y., Timmermann, R., Rodehacke, C. B., Schröder, M. & Hellmer, H. H. Modeling the spreading of glacial meltwater from the Amundsen and Bellingshausen Seas. *Geophys. Res. Lett.* **41,** 7942–7949 (2014).
12. Paolo, F. S., Fricker, H. A. & Padman, L. Volume loss from Antarctic ice shelves is accelerating. *Science* **348,** 327–331 (2015).
13. Drucker, R., Martin, S. & Kwok, R. Sea ice production and export from coastal polynyas in the Weddell and Ross Seas. *Geophys. Res. Lett.* **38,** L17502 (2011).
14. Sigman, D. M., Hain, M. P. & Haug, G. H. The polar ocean and glacial cycles in atmospheric CO_2 concentration. *Nature* **466,** 47–55 (2010).
15. Ferrari, R. *et al.* Antarctic sea ice control on ocean circulation in present and glacial climates. *Proc. Natl Acad. Sci. USA* **111,** 8753–8758 (2014).
16. Frölicher, T. L. *et al.* Dominance of the Southern Ocean in anthropogenic carbon and heat uptake in CMIP5 models. *J. Clim.* **28,** 862–886 (2015).
17. Landschützer, P. *et al.* The reinvigoration of the Southern Ocean carbon sink. *Science* **349,** 1221–1224 (2015).
18. Hellmer, H. H., Huhn, O., Gomis, D. & Timmermann, R. On the freshening of the northwestern Weddell Sea continental shelf. *Ocean Sci.* **7,** 305–316 (2011).
19. Saenko, O. A., Schmittner, A. & Weaver, A. J. On the role of wind-driven sea ice motion on ocean ventilation. *J. Phys. Oceanogr.* **32,** 3376–3395 (2002).
20. Komuro, Y. & Hasumi, H. Effects of surface freshwater flux induced by sea ice transport on the global thermohaline circulation. *J. Geophys. Res.* **108,** 3047 (2003).
21. Kirkman, C. H. & Bitz, C. M. The effect of the sea ice freshwater flux on Southern Ocean temperatures in CCSM3: deep-ocean warming and delayed surface warming. *J. Clim.* **24,** 2224–2237 (2011).
22. Dee, D. P. *et al.* The ERA-Interim reanalysis: configuration and performance of the data assimilation system. *Q. J. R. Meteorol. Soc.* **137,** 553–597 (2011).
23. Meier, W. *et al. NOAA/NSIDC Climate Data Record of Passive Microwave Sea Ice Concentration* v. 2, 1980–2009, http://dx.doi.org/10.7265/N55M63M1 (National Snow and Ice Data Center, accessed 20 June 2013).
24. Kurtz, N. T. & Markus, T. Satellite observations of Antarctic sea ice thickness and volume. *J. Geophys. Res.* **117,** C08025 (2012).
25. Massonnet, F. *et al.* A model reconstruction of the Antarctic sea ice thickness and volume changes over 1980–2008 using data assimilation. *Ocean Model.* **64,** 67–75 (2013).
26. Fowler, C., Emery, W. J. & Tschudi, M. A. *Polar Pathfinder Daily 25 km EASE-Grid Sea Ice Motion Vectors* v. 2, 1980–2009 (National Snow and Ice Data Center, accessed 14 April 2014).
27. Abernathey, R. P. *et al.* Water-mass transformation by sea ice in the upper branch of the Southern Ocean overturning. *Nat. Geosci.* **9,** 596–601 (2016).
28. Talley, L. D. Closure of the global overturning circulation through the Indian, Pacific, and Southern Oceans: schematics and transports. *Oceanography* **26,** 80–97 (2013).
29. Tamura, T., Ohshima, K. I., Nihashi, S. & Hasumi, H. Estimation of surface heat/salt fluxes associated with sea ice growth/melt in the Southern *Ocean. Sci. Online Lett. Atmos.* **7,** 17–20 (2011).
30. Massom, R. A. *et al.* Snow on Antarctic sea ice. *Rev. Geophys.* **39,** 413–445 (2001).

Acknowledgements This work was supported by ETH Research Grant CH2-01 11-1 and by European Union (EU) grant 264879 (CARBOCHANGE). I.F. was supported by C2SM at ETH Zürich and the Swiss National Science Foundation Grant P2EZP2-152133. S.K. was supported by the Center of Excellence for Climate System Analysis and Prediction (CliSAP), University of Hamburg, Germany. F.A.H. and S.K. acknowledge support from the International Space Science Institute (ISSI), Bern, Switzerland, under project #245. We are thankful to F. Massonnet for providing the sea-ice thickness reconstruction and discussion. The ICESat-1 sea-ice thickness data were provided by the NASA Goddard Space Flight Center. The ship-based sea-ice thickness data were provided by the SCAR Antarctic Sea Ice Processes and Climate (ASPeCt) programme. We appreciate the provision of sea-ice concentration and motion data by the National Snow and Ice Data Center, the Integrated Climate Data Center at the University of Hamburg and R. Kwok. We thank T. Frölicher, S. Yang, A. Stössel, M. Frischknecht, L. Papritz, P. Durack, M. van den Broecke, J. Lenaerts, J. van Angelen and M. Meredith for discussion, comments, and ideas.

Author Contributions F.A.H., M.M. and I.F. conceived the study. F.A.H. collated the data and performed the analyses. F.A.H. and N.G. wrote the manuscript. M.M., I.F. and S.K. assisted during the writing process. S.K. assisted in the quality and uncertainty assessment. All authors developed the methods and interpreted the results. N.G. and M.M. supervised this study.

Author Information Reprints and permissions information is available at www.nature.com/reprints. The authors declare no competing financial interests. Readers are welcome to comment on the online version of the paper. Correspondence and requests for materials should be addressed to F.A.H. (alexander.haumann@usys.ethz.ch).

Reviewer Information *Nature* thanks K. Ohshima and the other anonymous reviewer(s) for their contribution to the peer review of this work.

METHODS

Data. The satellite-derived sea-ice concentration is drawn from the Climate Data Record (CDR)[23], which comprises data from the NASA Team algorithm (NTA)[31] and the Bootstrap algorithm (BA)[32], as well as a merged data set. Sea-ice thickness data are taken from a reconstruction with the ocean–sea-ice model NEMO-LIM2 (1980–2009)[25], from the laser altimeter ICESat-1 (2003–2008; http://seaice.gsfc.nasa.gov)[24], as well as from ship-based observations (ASPeCt; 1980–2005; http://aspect.antarctica.gov.au)[33]. Satellite-derived sea-ice drift data originates from the National Snow and Ice Data Center (NSIDC)[26], is provided in NetCDF-format by the Integrated Climate Data Center (University of Hamburg) and is corrected by drifting buoy data (1989–2005)[34]. We used an alternative sea-ice drift product for the uncertainty estimation (1992–2003; http://rkwok.jpl.nasa.gov; hereafter referred to as Kwok *et al.*)[35,36]. Additionally, we used daily atmospheric sea-level pressure, surface air temperature and 10 m wind speed values from the ERA-Interim reanalysis (1980–2009, http://apps.ecmwf.int)[22]. We provide a detailed description of the data processing in the corresponding sections below.

Sea-ice concentration. We used all three sea-ice concentration products available from the CDR[23]. If any of the grid points in either the merged, NTA or BA products show a sea-ice concentration of 0%, all of the products are set to 0%. We used a first-order conservative remapping method from the Climate Data Operators (CDO)[37] to interpolate the sea-ice concentration to the sea-ice drift grid. The BA performs better than the NTA around Antarctica as the NTA underestimates sea-ice concentrations by 10% or more[23,38] (Extended Data Fig. 1a, b). Therefore, we primarily used the BA product. However, the BA potentially underestimates the concentration of sea ice in the presence of thin ice and leads[23,38]. Therefore, we used the merged product, which should be more accurate in these regions[23], to estimate the uncertainties. Generally, sea-ice concentration is the best constrained of the three sea-ice variables. Its contribution to the climatological mean flux uncertainty is below 1% (Extended Data Table 1). To obtain the uncertainty in the freshwater flux trends, we also used the NTA because differences in the trends in Antarctic sea-ice area between the BA and NTA have been reported[39]. Differences between the BA and NTA sea-ice concentration trends range from 10% to 20% relative to the actual trend (Extended Data Fig. 1c, d). The associated uncertainties in the spatially integrated sea-ice freshwater flux trends are about 10% (Extended Data Table 2).

Sea-ice thickness. Sea-ice thickness data spanning our entire analysis period do not exist, mostly owing to challenges in remote sensing of Antarctic sea-ice thickness[40]. We therefore used a sea-ice thickness reconstruction[25] from a model that assimilated the observed sea-ice concentration. Through this assimilation, the model constrained air–sea heat fluxes, improving the spatial and temporal variability of the sea-ice thickness. The model did not assimilate sea-ice thickness observations themselves. Sea-ice thickness, as we use it here, is not weighted with sea-ice concentration and does not include the snow layer.

The reconstruction overestimates the sea-ice thickness in the central Weddell and Ross seas and underestimates it in some coastal regions compared to the ICESat-1[24] and ASPeCt[33] data sets (Extended Data Fig. 2). To compare the different sea-ice thickness data sets, we interpolated the reconstruction, ICESat-1 and ASPeCt data to the sea-ice drift grid using CDO[37] distance-weighted averaging. For our best estimate of the sea-ice freshwater fluxes, we applied a weighted bias correction to the reconstruction using the spatially gridded version of the ICESat-1 data (see the following paragraph). Both the ICESat-1 and ASPeCt data sets are potentially biased low, particularly in areas with thick or deformed sea ice[33,40–42], where we found the largest differences between these two data sets and the uncorrected reconstruction. Thus, the thicker sea ice in the Weddell Sea in the uncorrected reconstruction might be realistic, especially when considering alternative ICESat-1 derived estimates for this region[40,43,44]. To capture the full uncertainty range associated with the mean sea-ice thickness distribution, we used the difference between the uncorrected reconstruction and the ICESat-1 data. Uncertainties in sea-ice thickness dominate the climatological freshwater flux uncertainties in the Atlantic and Indian Ocean sectors, ranging from 10% to 35%, and are also substantial in all other regions and for the overall trends (Extended Data Tables 1, 2).

For the correction of the mean sea-ice thickness distribution, we first calculated relative differences to ICESat-1 whenever data were available. Then, we averaged all of the differences that were within two standard deviations over time. We applied this average relative bias correction map to the data at each time step. To ensure that local extremes were not exaggerated, we used weights. Weights were one for a sea-ice thickness of 1.2 m, that is, the full bias correction was applied, and decreased to zero for sea-ice thicknesses of 0.2 m and 2.2 m, that is, no bias correction was applied. We derived these thresholds empirically to reduce biases with respect to the non-gridded ICESat-1 and ASPeCt data (Extended Data Fig. 2). Trends in the reconstruction remain largely unaffected by the bias correction (comparing Extended Data Fig. 2a and the original trend[25]).

Local extremes in the sea-ice thickness reconstruction, caused by ridging events, are probably inconsistent with the observed sea-ice drift and would lead to unrealistic short-term variations in our final fluxes. However, when considering the net annual melting and freezing fluxes and averages over large areas these variations cancel out. To reduce the noise in our data set, we filtered extremes with a daily sea-ice thickness anomaly larger than 2 m with respect to the climatological seasonal cycle, representing only 0.1% of all data points. These and other missing grid points (in total 2.6%) were interpolated by averaging the neighbouring grid points. We also calculated our sea-ice freshwater fluxes on the basis of the unfiltered data and included these fluxes in our uncertainty estimate.

Snow-ice formation due to flooding and refreezing[30,45] is part of the estimated sea-ice thickness. As snow-ice forms partly from the atmospheric freshwater flux and not from the ocean alone, it could lead to an overestimation of the total ocean to sea-ice freshwater flux due to freezing. The amount of snow-ice formation is highly uncertain[30,45] but lies within the uncertainty of the sea-ice thickness. To account for this process, we reduced the freezing fluxes according to snow-ice formation estimates from the literature[30]. In the Atlantic, Indian Ocean and Pacific sectors we applied approximate snow-ice formation rates of $8 \pm 8\%$, $15 \pm 15\%$, and $12 \pm 12\%$ of the freezing flux, respectively[30]. In the entire Southern Ocean, the amount of snow that is transformed to ice would thus amount to about 50 mSv, or about 35% of the suggested atmospheric freshwater flux onto Antarctic sea ice[27].

Trends in sea-ice thickness (Extended Data Fig. 2a) are highly uncertain but broadly agree among different modelling studies[25,46,47]. To show that our results are robust with respect to the less certain trends or short-term variations in sea-ice thickness, we compared our estimated transport trends across the latitude bands (equation (3)) with a sensitivity analysis, where we kept the sea-ice thickness constant. The resulting transport trends across the latitude bands of about −6 mSv per decade in the Atlantic sector and about +11 mSv per decade in the Pacific sector are still within our estimated uncertainty (Extended Data Table 2). Most of the sea-ice thickness trends (Extended Data Fig. 2a) occur either north (in the Pacific sector) or south (in the Atlantic sector) of the zero freshwater flux line or latitude bands. Thus, the trend in sea-ice thickness does not considerably affect the northward sea-ice freshwater transport trend. However, the mean sea-ice thickness uncertainty at the zero freshwater flux line is the largest contributor to the overall northward sea-ice freshwater transport trend (Extended Data Table 2).

Sea-ice drift. We used the gridded version of the NSIDC[26] sea-ice drift data set. In the Antarctic, it is based on five passive microwave sensors[48,49] and data from the Advanced Very High Resolution Radiometer (AVHRR)[50] (Extended Data Fig. 4). Two studies validated this data set with buoy data in the Weddell Sea (1989–2005)[34] and around East Antarctica (1985–1997)[51]. There is a very high correlation between the buoy and the satellite data on large temporal and spatial scales (that is, monthly and regional) and a strongly reduced agreement on smaller scales (that is, daily and local)[34,51]. The satellite-derived sea-ice drift underestimates the sea-ice velocity given by the buoys by 34.5%[34], that is, faster drift velocities have a larger bias[52]. The bias is smaller for the meridional (26.3%) than for the zonal drift[34]. We corrected for these low biases by multiplying the drift velocity by the correction factor (1.357) that corresponds to the meridional drift bias[34]. We argue that the meridional component of the bias is the better estimate in the central sea-ice region, which is the key region for our results. Here, the drift is mainly meridional. The larger biases are observed in the swift, mostly zonal drift along the sea-ice edge that causes the larger zonal biases. The spatial dependence of the bias and our correction imply that larger biases and uncertainties remain in our final product around the sea-ice edge.

We processed this bias-corrected drift data further: first we removed all of the data that were flagged as close to the coast or interpolated over large distances in the product; second, we removed any data with sea-ice concentrations below 50%, closer than 75 km to the coast[34], or with a spurious, exact value of zero. Our results are not sensitive to this filtering but it reduces the spatial and temporal noise. After these modifications, about 75% of all of the grid cells covered by sea ice had an associated drift vector.

We compared both the original and the bias-corrected data to a partly independent product by Kwok *et al.*[35,36]. We interpolated these data onto our grid using CDO[37] distance-weighted averaging and applied the same 21-d running mean as for the NSIDC sea-ice drift data. We compared sea-ice drift vectors whenever both data sets were available and sea-ice concentrations were larger than 50%. Extended Data Fig. 3 shows the meridional drift components before and after applying the bias correction factor from the buoy data (Extended Data Fig. 3a and b, respectively). We find that the agreement between the two data sets is much higher after the corrections. Compared with the original NSIDC sea-ice drift data set, the largest improvement occurs in the slope: 1.06 compared with 1.55. Root-mean-square (r.m.s.) differences and the linear correlation coefficient remain identical and the absolute bias is reduced by 0.2 km d^{-1}. The correlation

coefficients between the two data sets are 0.8 for both the zonal and meridional drift components. The spatial patterns of the mean annual sea-ice drift speed (Extended Data Fig. 3c–e) illustrate the improvement in agreement between the two data sets after the application of the bias correction but confirm that considerable differences remain at the sea-ice edge. These differences lead to a relatively high r.m.s. difference in the annual mean sea-ice drift speed in these regions (Extended Data Fig. 3f). However, in the central sea-ice pack—the region that is crucial for our results—the r.m.s. differences are much smaller.

Our bias-corrected sea-ice drift speeds are typically slightly lower (by about 9–19%) than those by Kwok *et al.* but considerably higher than in the uncorrected NSIDC data (about 26%, see above). We used these differences between the data sets to estimate the uncertainties induced by sea-ice drift on the sea-ice freshwater transport (Δu; Extended Data Tables 1, 2). First, we recomputed all of the fluxes by correcting the original NSIDC data with correction factors derived from the Kwok *et al.* data (1.82 or 45% for the zonal drift, and 1.55 or 35% for the meridional drift) instead of the buoy-derived correction factor. In this way, we also accounted for an uncertainty in the drift direction. Then we averaged the deviations between our best estimate and the estimate based on Kwok *et al.*[35,36] with those between our best estimate and using the uncorrected and unfiltered NSIDC data. Uncertainties from sea-ice drift in the freshwater fluxes are about 20%. They contribute considerably to the final freshwater flux uncertainty and our trend uncertainties in all regions.

Sea-ice–ocean freshwater flux. We estimated annual net sea-ice–ocean freshwater fluxes over the period 1982–2008 by calculating the local sea-ice volume change and divergence[8,53]. From this we derived the local freshwater fluxes F ($m^3\ s^{-1}$) from the sea ice to the ocean due to freezing and melting on a daily basis through a mass balance:

$$F = -C_{fw}\left(\frac{\partial(Ach)}{\partial t} + \nabla\cdot(Ach\boldsymbol{u})\right) \quad (1)$$

where the four variables c, h, $\boldsymbol{u}$ and A denote the sea-ice concentration, thickness, drift velocity and grid-cell area, respectively. The factor C_{fw} converts the sea-ice volume flux to a freshwater equivalent[54]:

$$C_{fw} = \frac{\rho_{ice}(1 - s_{ice}/s_{sw})}{\rho_{fw}} \quad (2)$$

Here, ρ_{ice}, s_{ice}, s_{sw} and ρ_{fw} are the sea-ice density ($925\ kg\ m^{-3}$)[55], the sea-ice salinity ($6\ g\ kg^{-1}$)[56], the reference seawater salinity ($34.7\ g\ kg^{-1}$)[28] and the freshwater density ($1{,}000\ kg\ m^{-3}$), respectively.

The annual sea-ice freshwater fluxes were computed from the daily fluxes from March to February of the next year (that is, March 1982 to February 2009), which correspond to the annual freezing and melting cycle of sea ice in the Southern Ocean[53]. Remaining imbalances between, for example, the open and coastal ocean of the Atlantic sector (Extended Data Tables 1, 2) are due to multiyear sea ice in the coastal region. We performed all of the calculations on the grid of the sea-ice drift data[26] and averaged all data products over 3×3 grid boxes, resulting in a nominal resolution of 75 km. To obtain the zero freshwater flux contour line, we averaged the climatological fluxes over 9×9 grid boxes. To estimate the melting and freezing fluxes, we separately summed up the positive and negative daily fluxes over a year (Fig. 4a, b). As temporal fluctuations accumulate when only adding positive or negative values, noise can lead to an overestimation of these fluxes. Each of the sea-ice variables (c, h and $\boldsymbol{u}$) were therefore low-pass filtered using a 21-d running mean.

Sea-ice freshwater transport. The total northward sea-ice volume transport (in $m^3\ s^{-1}$) between the coastal and open ocean regions equals the spatial integral of the divergence term in equation (1) in either of the two regions (by Gauss's theorem). We chose the open ocean region because there is considerable zonal exchange between the Indian Ocean and Atlantic sectors (Fig. 2a) in the coastal region, influencing the sector-based estimates. In the open ocean, this effect is negligible. We used this approach for the reported transport estimates (Extended Data Tables 1–3 and Extended Data Fig. 5a–c).

To demonstrate that our main findings are robust on the basin scale, and not influenced by small-scale noise and local uncertainties, we also calculated the northward sea-ice freshwater transport across latitude bands at 69.5° S in the Atlantic sector and 71° S in the Pacific sector (Fig. 3). To this end, we averaged c_n, h_n and meridional drift (v_n) in 1° longitude segments (n) along these latitudes and calculated the local freshwater transport T_n ($m^3\ s^{-1}$):

$$T_n = C_{fw} c_n h_n v_n \Delta l_n \quad (3)$$

where Δl_n denotes the length of sectors n along the latitude bands. The combined annual northward freshwater transport of both sectors is 100 ± 30 mSv with an increase of 8 ± 5 mSv per decade over the period 1982–2008 (Extended Data Fig. 5d and Fig. 3). This compares well with the mean (120 ± 30 mSv) and trend (9 ± 5 mSv per decade) of our spatially integrated sea-ice–ocean fluxes in the Pacific and Atlantic (Extended Data Fig. 5b, c).

We calculated the spatial pattern of the sea-ice freshwater transport $\boldsymbol{f}$ ($m^2\ s^{-1}$) as displayed in Fig. 2a, c, according to:

$$\boldsymbol{f} = C_{fw} ch\boldsymbol{u} \quad (4)$$

Time-series homogenization. Our analysis and earlier studies[9,57] revealed major temporal inhomogeneities in the NSIDC sea-ice drift data set at the transitions between satellite sensors (Extended Data Fig. 4). We argue that these temporal inhomogeneities are linked to the unavailability of the 85 GHz and 91 GHz channels and sparser data coverage in the earlier years. The drift speed before 1982 seems to be underestimated, which is to some extent mitigated by AVHRR data thereafter. From 1982 to 1986, the drift speed is consistent but has a low bias. The drift ramps up in 1987, when the 85 GHz channels became available, and decreases again between 1989 and 1991, when these channels degraded[58]. A final sudden decrease occurs from 2005 to 2006 when 85 GHz data were not used. We used wind speed data over the sea ice from ERA-Interim[22] as an independent data source and scaled it to the sea-ice drift velocity for comparison (Extended Data Figs 4b). The scaling factor stems from the consistent years in the period 1988–2008 and varies in space and with the season[59,60]. This analysis supports our argument that the sea-ice drift speed is underestimated when the higher resolution 85/91 GHz channels were not available. We note that the meridional drift seems less sensitive to these inhomogeneities than the total drift, which might be related to higher data availability in the central sea-ice pack and is consistent with the lower biases found in the meridional sea-ice drift.

Spurious increases in the sea-ice velocity would affect our estimated trends if they were not taken into account (Extended Data Figs 5, 6). Thus, we corrected the annual divergence (equation (1)) and lateral transport (equations (3), (4)) for the sensor-related temporal inconsistencies as follows. We excluded the inconsistent years (1980, 1981, 1987, 1989–1991, 2005 and 2006) from the analysis. To homogenize the years 1982–1986 with the years 1988–2008, that is, to remove the spurious trend in 1987, we first calculated linear regression lines before and after 1987 at each grid point. Then we added the differences between the end (1986) and start (1988) points of the regression lines to all years before 1987, that is, assuming a zero change in 1987. Fitting regressions before and after spurious jumps is a common procedure to homogenize climate data[61,62]. Here, we used a linear regression that serves the purpose of computing long-term trends in the time series.

To estimate the sensitivity of the trends in northwards sea-ice freshwater transport to the uncertainties associated with the offset correction before 1987 (shown in orange and green in Extended Data Fig. 5), we performed a Monte Carlo analysis by varying the offset and estimating the resulting trends. We generated 10,000 normally distributed offsets around our best guess (about 19 ± 5 mSv for the entire Southern Ocean; Extended Data Table 3). The standard deviation of this distribution was chosen to match the offset uncertainty that arises from the r.m.s. errors of the trends in each of the two time intervals: 1982–1986 and 1988–2008. For each of these generated offsets, we then estimated the trends and their significance (Extended Data Table 3). For both the entire Southern Ocean and the Pacific sector, all of the sampled offsets yield a positive northward sea-ice freshwater transport trend. All trends for the Pacific sector and 92% of those for the entire Southern Ocean are positive and at the same time significant at least at a 90% confidence level using Student's t-test. Thus, our trend results are insensitive to uncertainties in the applied homogenization at the 90% confidence level. The posterior uncertainty shows that the uncertainty associated with the offset has no noticeable effect on the total uncertainty range, that is, is smaller than ± 1 mSv per decade.

Uncertainty estimation. The uncertainties of the local (grid-point-based) fluxes and timescales shorter than one year are probably large due to potential inconsistencies between the data sets on such scales and an amplification of the uncertainties by the spatial and temporal differentiations in equation (1). Integrating these terms in space and time greatly reduces these uncertainties (Extended Data Tables 1, 2). We estimated the uncertainties in our product that are associated with the underlying input variables c, h and $\boldsymbol{u}$ by using their observationally constrained ranges from different data sources, including the applied corrections and filtering as described. Additionally, we used an averaging period of 31 d (instead of 21 d) and, for trends only, an estimate without a running-mean filter, to obtain uncertainty estimates associated with temporal noise (Δt). The results confirmed that the annual melting or freezing fluxes, are sensitive to the low-pass filtering, but not the net annual fluxes, as in the latter product the noise is averaged out. The sensitivity of the spatially integrated values to variations of the zero freshwater flux line is estimated by varying the smoothing radius from two to six grid boxes (ΔA). The uncertainty associated with the constant conversion factor (ΔC_{fw}; equation (2))

is about 5% when using a realistic range of values[28,55,56]. For the trends only we computed the standard error of the slope from the variance of the residuals around the regression line (Δs_e)[63]. The total uncertainty for both the climatological mean and the trends was estimated by calculating the r.m.s. of the individual contributions. This analysis shows that in the Atlantic and Indian Ocean sectors both the uncertainties in the climatology and trends (Extended Data Tables 1, 2) are dominated by uncertainties in the sea-ice thickness. In contrast, the uncertainty in the sea-ice drift dominates the uncertainty in the Pacific sector. We tested the significance of the trends with Student's *t*-test, accounting for the fact that only 21 out of 27 years were used and for a lag-1 autocorrelation[63]. To indicate the significance of the trends at grid-point level (Fig. 2c, d and Extended Data Fig. 6), at which the data uncertainties are unknown, the local r.m.s. of the variance of the residuals was artificially increased by 40%, approximately corresponding to our data uncertainty estimate in Extended Data Table 2. The quality of our data directly at the coastline and around the sea-ice edge is reduced due to the limited quality and quantity of the underlying observations in these regions.

Sea-ice freshwater flux evaluation. A modelling study[27] carried out in parallel to this study calculated freshwater fluxes associated with sea-ice formation, melting and transport in the Southern Ocean State Estimate (SOSE). This model assimilates a large amount of observational data and optimizes the surface fluxes. They estimated an annual sea-ice–ocean freshwater flux due to sea-ice formation of −360 mSv over the entire Southern Ocean, which is within our estimated range of -410 ± 110 mSv. Moreover, they estimated that the combined annual sea-ice–ocean freshwater flux due to sea-ice and snow melting is about 500 mSv. Thus, in their estimate a total of 140 mSv of snow accumulated on the sea ice. Our estimates partly include snow accumulation on sea ice, because part of the sea-ice thickness results from snow-ice formation, which we estimated to be about −50 mSv (section on sea-ice thickness). However, the snow layer on top of the sea ice is not included in our estimate of the freshwater flux due to sea-ice melting of 460 ± 100 mSv. In that study[27], the authors estimate that the lateral sea-ice freshwater transport from the density class of the CDW to the AAIW and the SAMW amounts to 200 mSv in the period between 2005 and 2010. Their estimate slightly differs from our estimated transport from the coastal to the open ocean, which ranges between about 140 mSv and 160 mSv in 2007 and 2008 (Extended Data Fig. 5). The reasons might be the slightly different regions and that their estimate also includes the transport of the snow layer on top of the sea ice.

Given the reduced confidence in the local fluxes (for example, sea-ice production in coastal polynyas), it is reassuring that our data agree within our estimated range of uncertainty with previous estimates of mean fluxes for some larger coastal polynya regions[64,65]. Our confidence is higher for fluxes integrated over larger regions, such as the high-latitude Ross and Weddell seas (Extended Data Fig. 5e). Here our estimates are in close agreement with previous studies.

In the Ross Sea, we estimated that the northward transport from the coastal region across a flux gate between Land Bay and Cape Adare[36] (the turquoise area in Extended Data Fig. 5e) is 23 ± 5 mSv, increasing by about 30% (or $+7 \pm 4$ mSv) per decade in the period 1992–2008. On the basis of the same passive microwave data, but using a different algorithm for retrieving the sea-ice motion data, two studies[36,66] found a mean sea-ice area flux across this flux gate of about 1,000,000 km^2 between March and November in the periods 1992–2003 (ref. 36) and 1992–2008 (ref. 66), respectively. Using an approximated mean sea-ice thickness (0.6 m)[13,66] and the conversion factor (equation (2)), this corresponds to a mean northward freshwater transport of about 19 mSv. In close agreement with our estimate, these studies found an increase of 30% per decade (about +6 mSv per decade). Another study[13], using sea-ice motion from the Advanced Microwave Scanning Radiometer-EOS (AMSR-E), estimated that the mean sea-ice area flux between April and October (2003–2008) across the same flux gate is about 9.3×10^5 km^2 corresponding to a freshwater transport of about 23 mSv. Using the same data, but an alternative approach[67], they found that the total sea-ice production in all of the Ross Sea polynyas together was about 737 km^3 between April and October (2003–2008), corresponding to a sea-ice–ocean freshwater flux of −31 mSv. This estimate is similar to the total production of about -36 ± 7 mSv south of the flux gate in our data set, because most of the sea-ice production in this region occurs in the polynyas[13]. Using passive microwave data, the same study[13] found an increase of the production in the Ross Sea polynyas of 28% per decade between 1992 and 2008. A modelling study[68] found a net annual sea-ice–ocean freshwater flux due to melting and freezing of −27 mSv on the continental shelf in the Ross Sea, which is in agreement with our estimate of -23 ± 5 mSv. They also found a long-term (unquantified, see figure 9b in ref. 68) decrease in the net annual sea-ice–ocean freshwater flux over the Ross Sea continental shelf in the period 1963–2000, which is qualitatively in line with our results.

In the Weddell Sea, the northward sea-ice area flux across a flux gate close to the 1,000 m isobath (blue area in Extended Data Fig. 5e) has been found to be 5.2×10^5 km^2 on the basis of AMSR-E data between April and October (2003–2008)[13]. Using an approximated mean sea-ice thickness (0.75 m)[13] and the conversion factor (2), this corresponds to a mean northward freshwater transport of about 16 mSv. This agrees well with our estimate of an annual northward transport of 16 ± 4 mSv for the same years and the same region. Similar to the Ross Sea, production in the major polynyas of the Weddell Sea was estimated[13]. However, in the Weddell Sea, a large fraction of the sea-ice transported across the flux gate is not produced in the coastal polynyas[13]; thus we cannot directly compare our large-scale estimate to the sea-ice production in the polynyas. In the same study[13], based on passive microwave data, they found a small, but insignificant long-term decrease in the sea-ice production in the Weddell Sea polynyas between 1992 and 2008, which is qualitatively consistent with our findings in the Atlantic sector. For a much larger area in the Weddell Sea, a modelling study[69] estimated an annual northward sea-ice freshwater transport of about 34 mSv and another observational study[70], mostly based on moorings and wind speed, estimated that this flux is as large as about 38 ± 15 mSv. These estimates agree well with our finding of an annual northward freshwater transport of 41 ± 18 mSv across the 69.5° S latitude band, which is approximately their considered transect.

Sea-ice freshwater transport based on ERA-Interim data. To support our findings, we quantified the changes in sea-ice motion that are induced by changes in geostrophic winds[59,60,70,71] from daily ERA-Interim[22] sea-level pressure and surface air temperature data. We averaged the data over 1° longitudinal segments along the previously defined latitude bands (Fig. 3), computed 21-d running means, and smoothed the data spatially over seven longitudinal bins. Then we calculated the sea-level pressure gradients along the latitude bands and used these together with the atmospheric surface density to estimate geostrophic winds normal to the latitude bands[59,71]. From these, we calculated the sea-ice drift speed using a drift-to-wind-speed ratio of 0.016, derived from drifting buoys in the central Weddell Sea[59,71]. This parameter is strongly variable in space and time, which is a major uncertainty in the resulting sea-ice drift. Nevertheless, it provides an average estimate for the mostly free drifting sea ice in the central Antarctic sea-ice pack[59,71].

The resulting northward sea-ice freshwater transport (equation (3)) is independent in terms of the sea-ice drift but not in terms of the sea-ice concentration and thickness. We used anomalies (at each 1° increment) because the absolute values of the local transport are likely to be biased by the local influences of ocean currents and sea-ice properties. The resulting total annual anomalies of the northward sea-ice freshwater transport agree well in terms of the variability and long-term trend with the transport anomalies based on the satellite sea-ice drift data (+8 mSv per decade; Fig. 3). These estimates do not suffer from the temporal inhomogeneities that we identified in the satellite sea-ice drift data (see Methods section 'Time-series homogenization').

Sea-ice contribution to ocean salinity. We determined the evolution of ocean salinity s (g kg^{-1}) in response to a given value of F (m^3 s^{-1}) from a combination of mass and salt balances. The mass balance for a given well-mixed ocean surface box of volume V and density ρ reads:

$$\frac{\mathrm{d}\rho V}{\mathrm{d}t} = \rho_{\mathrm{in}} Q_{\mathrm{in}} + \rho_{\mathrm{fw}} F - \rho Q_{\mathrm{out}} \tag{5}$$

where Q_{in} and Q_{out} (m^3 s^{-1}) are the volume fluxes of seawater in and out of the box, ρ_{in} (kg m^{-3}) is the respective density. In a steady state, equation (5) yields:

$$\rho_{\mathrm{in}} Q_{\mathrm{in}} = \rho Q_{\mathrm{out}} - \rho_{\mathrm{fw}} F \tag{6}$$

The corresponding salt balance reads:

$$\rho V \frac{\mathrm{d}s}{\mathrm{d}t} = \rho_{\mathrm{in}} Q_{\mathrm{in}} s_{\mathrm{in}} - \rho Q_{\mathrm{out}} s \tag{7}$$

We assumed the same constant source water salinity $s_{\mathrm{in}} = s_{\mathrm{sw}}$ and ρ_{fw} as in equation (2) and used a constant reference density ($\rho = 1{,}027$ kg m^{-3}). Moreover, we used the formation rate of the modified water mass as the volume flux of seawater out of the surface box ($Q_{\mathrm{out}} = Q$). Then, substituting equation (6) into equation (7) yields:

$$\rho V \frac{\mathrm{d}s}{\mathrm{d}t} = (\rho Q - \rho_{\mathrm{fw}} F) s_{\mathrm{sw}} - \rho Q s \tag{8}$$

In a steady state, this results in an equation that describes the modified salinity s as follows:

$$\rho Q s = (\rho Q - \rho_{\mathrm{fw}} F) s_{\mathrm{sw}} \tag{9}$$

Using $s = s_{\mathrm{sw}} + \Delta s$, where Δs is the difference in salinity between the source and modified water masses, equation (9) reduces to:

$$\Delta s = -\frac{\rho_{\mathrm{fw}} s_{\mathrm{sw}} F}{\rho Q} \tag{10}$$

We used net water-mass formation rates (Q) of 29 Sv for formation of the AABW from the CDW and 13 Sv for the formation of the AAIW/SAMW from the CDW[28]. Figure 1a illustrates the results and shows the zonal mean ocean salinity and density distribution[72] for comparison.

Assuming that $+130 \pm 30$ mSv of freshwater enter the CDW through northward sea-ice freshwater transport, the salinity modification between the CDW and AAIW/SAMW (using equation (10)) is $-0.33 \pm 0.09\,\mathrm{g\,kg^{-1}}$. The uncertainty includes a ± 2 Sv uncertainty in the water-mass formation rate. In observations, the salinity difference between the CDW and the AAIW and SAMW ranges from about $-0.3\,\mathrm{g\,kg^{-1}}$ to $-0.5\,\mathrm{g\,kg^{-1}}$ (ref. 28). Thus, northward freshwater transport by sea-ice could explain the majority of the salinity modification, consistent with very recent findings[27] and a mixed-layer salinity budget[73].

Similarly, we calculated the contribution of -130 ± 30 mSv of freshwater removed from coastal regions due to northward sea-ice transport to the salinity modification (using equation (10)) between the CDW and AABW, obtaining an increase of $+0.15 \pm 0.06\,\mathrm{g\,kg^{-1}}$. The uncertainty includes a ± 7 Sv uncertainty in the AABW formation. However, the observed salinity differences between the CDW and AABW are generally small or even of opposite sign[74]. This is the result of a compensating effect between a sea-ice-driven salinification and a freshening from glacial and atmospheric freshwater. The freshwater fluxes from land ice through basal and iceberg melting are about $+46 \pm 6$ mSv and $+42 \pm 5$ mSv, respectively[75]. Assuming that roughly 60% of the icebergs melt in the coastal regions[76], a total of about $+70$ mSv are added from the land ice to the coastal ocean, corresponding to a freshening of about $-0.08\,\mathrm{g\,kg^{-1}}$ or a compensation of the sea-ice freshwater flux of about 55% in the AABW. We estimated from the ERA-Interim atmospheric reanalysis data[22] that the net atmospheric freshwater flux in the coastal region is about $+80$ mSv, corresponding to a freshening of about $-0.09\,\mathrm{g\,kg^{-1}}$. The resulting net salinity change in coastal waters from sea-ice, atmospheric and land-ice freshwater fluxes is almost zero ($-0.02\,\mathrm{g\,kg^{-1}}$). Such a compensation of the freshwater fluxes in coastal regions was noticed previously[69,77]. We note that large regional variations of these fluxes have been reported[75,78].

To estimate the temporal salinity changes at the surface and in the newly formed AAIW and SAMW, we assumed a constant value of Q and that the freshwater flux and ocean salinity consist of a climatological value plus a time-dependent perturbation ($\overline{F} + F'$ and $\overline{s} + s'$, respectively). Equation (8) then yields:

$$\rho V \frac{\mathrm{d}s'}{\mathrm{d}t} = \rho Q s_{\mathrm{sw}} - \rho_{\mathrm{fw}} s_{\mathrm{sw}} \overline{F} - \rho Q \overline{s} - \rho_{\mathrm{fw}} s_{\mathrm{sw}} F' - \rho Q s' \tag{11}$$

As the climatological fluxes are in steady state, the first three terms on the right side in equation (11) cancel according to equation (9), resulting in:

$$\rho V \frac{\mathrm{d}s'}{\mathrm{d}t} = -\rho_{\mathrm{fw}} s_{\mathrm{sw}} F' - \rho Q s' \tag{12}$$

We approximated the freshwater flux perturbation ($F' = at$) using our estimated trend a, and rearranged the terms resulting in a first-order linear differential equation:

$$\frac{\mathrm{d}s'}{\mathrm{d}t} + \frac{Q}{V} s' = -\frac{\rho_{\mathrm{fw}} s_{\mathrm{sw}} a}{\rho V} t \tag{13}$$

Integration in time yields an expression for the time-dependent evolution of the salinity perturbation:

$$s' = -\frac{\rho_{\mathrm{fw}} s_{\mathrm{sw}} a}{\rho Q} \left(t - \frac{V}{Q} + \frac{V}{Q} \mathrm{e}^{-\frac{Q}{V} t} \right) \tag{14}$$

To obtain an estimate of the salinity trend at a given time t, we substituted equation (14) into equation (13) as follows:

$$\frac{\mathrm{d}s'}{\mathrm{d}t} = \frac{\rho_{\mathrm{fw}} s_{\mathrm{sw}} a}{\rho Q} \left(\mathrm{e}^{-\frac{Q}{V} t} - 1 \right) \tag{15}$$

The equilibrium response of the system, that is, the long-term trend after several years of perturbation, is:

$$\lim_{t \to \infty} \frac{\mathrm{d}s'}{\mathrm{d}t} = -\frac{\rho_{\mathrm{fw}} s_{\mathrm{sw}} a}{\rho Q} \tag{16}$$

Using our estimated sea-ice freshwater transport trend (a) of $+9 \pm 5$ mSv per decade and an AAIW/SAMW water-mass formation rate as above, we obtained an equilibrium freshening rate of $-0.023 \pm 0.014\,\mathrm{g\,kg^{-1}}$ per decade (green in Extended Data Fig. 7b), which is valid for sufficiently large values of Qt/V.

Extended Data Fig. 7b (in purple and blue; using equation (14)) shows that if we assumed that the trend started in 1982, there would be a delayed response lowering the mean salinity trend estimate depending on V. We thus tested the sensitivity of the trend to V, which corresponds to the upper 150 m between the zero sea-ice-ocean freshwater flux line and the Subantarctic Front[79] (Extended Data Fig. 7a), which is the source region of the AAIW. The circumpolar V of about $5 \times 10^6\,\mathrm{km^3}$ results in a mean salinity trend (using equation (14)) of $-0.014 \pm 0.008\,\mathrm{g\,kg^{-1}}$ per decade between 1982 and 2008 (purple). However, the AAIW formation does not occur in a circumpolar belt but mostly in the south-eastern Pacific and north-western Atlantic, that is, on either side of Drake Passage[80–84]. Assuming that most of the water is modified in this region and further downstream in the South Pacific[80,82,84], we estimated a second, somewhat smaller V of about $2 \times 10^6\,\mathrm{km^3}$ (shown in blue). The sea-ice freshwater transport trend into this reference volume is about $+8 \pm 5$ mSv per decade (Figs 2c, d), resulting in a mean salinity trend (using equation (14)) of $-0.018 \pm 0.010\,\mathrm{g\,kg^{-1}}$ per decade (blue); because a certain amount of freshwater is transported eastwards out of this sector (blue), the mean trend of the delayed response lies somewhere in between the estimates based on the two different reference volumes (blue and purple).

It is unlikely that the trend started exactly in 1982. Thus, the actual salinity response will fall between our estimated delayed response and the equilibrium response. For the range of values above, the deviations in the freshening rate due to effects of a delay and variations in the reference volume are much smaller than the actual magnitude of the trend itself. We thus conclude that the overall mean freshening rate of the newly formed AAIW and the surface waters advected northwards across the Subantarctic Front into the SAMW due to the changes in sea-ice freshwater transport is about $-0.02 \pm 0.01\,\mathrm{g\,kg^{-1}}$ per decade (Fig. 1b).

Data deposition. Sea-ice freshwater fluxes leading to the main conclusions are publicly available (http://dx.doi.org/10.16904/8). Other presented data are available from the corresponding author upon request.

Code availability. Climate Data Operators (CDO; version 1.6.8) used for part of the analysis is publicly available (http://www.mpimet.mpg.de/cdo). Other analytical scripts are available upon request from the corresponding author.

31. Cavalieri, D. J. & Parkinson, C. L. Antarctic sea ice variability and trends, 1979–2006. *J. Geophys. Res.* **113,** C07004 (2008).
32. Comiso, J. C. Characteristics of Arctic winter sea ice from satellite multispectral microwave observations. *J. Geophys. Res.* **91,** 975–994 (1986).
33. Worby, A. P. *et al.* Thickness distribution of Antarctic sea ice. *J. Geophys. Res.* **113,** C05S92 (2008).
34. Schwegmann, S., Haas, C., Fowler, C. & Gerdes, R. A comparison of satellite-derived sea-ice motion with drifting-buoy data in the Weddell Sea, Antarctica. *Ann. Glaciol.* **52,** 103–110 (2011).
35. Kwok, R., Schweiger, A., Rothrock, D. A., Pang, S. & Kottmeier, C. Sea ice motion from satellite passive microwave imagery assessed with ERS SAR and buoy motions. *J. Geophys. Res.* **103,** 8191–8214 (1998).
36. Kwok, R. Ross sea ice motion, area flux, and deformation. *J. Clim.* **18,** 3759–3776 (2005).
37. *Climate Data Operators* v. 1.6.8. (CDO, 2015); http://www.mpimet.mpg.de/cdo.
38. Comiso, J. C., Cavalieri, D. J., Parkinson, C. L. & Gloersen, P. Passive microwave algorithms for sea ice concentration: A comparison of two techniques. *Remote Sens. Environ.* **60,** 357–384 (1997).
39. Eisenman, I., Meier, W. N. & Norris, J. R. A spurious jump in the satellite record: has Antarctic sea ice expansion been overestimated? *Cryosphere* **8,** 1289–1296 (2014).
40. Kern, S. & Spreen, G. Uncertainties in Antarctic sea-ice thickness retrieval from ICESat. *Ann. Glaciol.* **56,** 107–119 (2015).
41. Kwok, R. & Maksym, T. Snow depth of the Weddell and Bellingshausen sea ice covers from IceBridge surveys in 2010 and 2011: an examination. *J. Geophys. Res.* **119,** 4141–4167 (2014).
42. Williams, G. *et al.* Thick and deformed Antarctic sea ice mapped with autonomous underwater vehicles. *Nat. Geosci.* **8,** 61–67 (2015).
43. Yi, D., Zwally, H. J. & Robbins, J. W. ICESat observations of seasonal and interannual variations of sea-ice freeboard and estimated thickness in the Weddell Sea, Antarctica (2003-2009). *Ann. Glaciol.* **52,** 43–51 (2011).
44. Kern, S., Ozsoy-Çiçek, B. & Worby, A. Antarctic sea-ice thickness retrieval from ICESat: Inter-comparison of different approaches. *Remote Sens.* **8,** 538 (2016).
45. Maksym, T. & Markus, T. Antarctic sea ice thickness and snow-to-ice conversion from atmospheric reanalysis and passive microwave snow depth. *J. Geophys. Res.* **113,** C02S12 (2008).
46. Zhang, J. Modeling the impact of wind intensification on Antarctic sea ice volume. *J. Clim.* **27,** 202–214 (2014).
47. Holland, P. R. *et al.* Modeled trends in Antarctic sea ice thickness. *J. Clim.* **27,** 3784–3801 (2014).
48. Emery, W. J., Fowler, C. W. & Maslanik, J. A. in *Oceanographic Applications of Remote Sensing* (eds Ikeda, M. & Dobson, F. W.) 367–379 (CRC Press, 1995).
49. Emery, W. J., Fowler, C. W. & Maslanik, J. A. Satellite-derived maps of Arctic and Antarctic sea ice motion: 1988 to 1994. *Geophys. Res. Lett.* **24,** 897–900 (1997).

50. Maslanik, J. *et al.* AVHRR-based Polar Pathfinder products for modeling applications. *Ann. Glaciol.* **25,** 388–392 (1997).
51. Heil, P., Fowler, C. W., Maslanik, J. A., Emery, W. J. & Allison, I. A comparison of East Antartic sea-ice motion derived using drifting buoys and remote sensing. *Ann. Glaciol.* **33,** 139–144 (2001).
52. Sumata, H. *et al.* An intercomparison of Arctic ice drift products to deduce uncertainty estimates. *J. Geophys. Res.* **119,** 4887–4921 (2014).
53. Haumann, F. A. *Dynamical Interaction Between Atmosphere and Sea Ice In Antarctica*. MSc thesis, Utrecht University (2011).
54. Ohshima, K. I., Nakanowatari, T., Riser, S., Volkov, Y. & Wakatsuchi, M. Freshening and dense shelf water reduction in the Okhotsk Sea linked with sea ice decline. *Prog. Oceanogr.* **126,** 71–79 (2014).
55. Timco, G. W. & Frederking, R. M. W. A review of sea ice density. *Cold Reg. Sci. Technol.* **24,** 1–6 (1996).
56. Vancoppenolle, M., Fichefet, T. & Goosse, H. Simulating the mass balance and salinity of Arctic and Antarctic sea ice. 2: importance of sea ice salinity variations. *Ocean Model.* **27,** 54–69 (2009).
57. Olason, E. & Notz, D. Drivers of variability in Arctic sea-ice drift speed. *J. Geophys. Res.* **119,** 5755–5775 (2014).
58. Wentz, F. J. *User's Manual: SSM/I Antenna Temperature Tapes Revision 1*. Report No. 120191 (Remote Sensing Systems, 1991).
59. Thorndike, A. S. & Colony, R. Sea ice motion in response to geostrophic winds. *J. Geophys. Res.* **87,** 5845–5852 (1982).
60. Kimura, N. Sea ice motion in response to surface wind and ocean current in the Southern Ocean. *J. Meteorol. Soc. Jpn* **82,** 1223–1231 (2004).
61. Peterson, T. C. *et al.* Homogeneity adjustments of in situ atmospheric climate data: a review. *Int. J. Climatol.* **18,** 1493–1517 (1998).
62. Aguilar, E., Auer, I., Brunet, M., Peterson, T. C. & Wieringa, J. *Guidelines on Climate Metadata and Homogenization.* Report No. WCDMP-53 (World Meteorological Organization, 2003).
63. Santer, B. D. *et al.* Statistical significance of trends and trend differences in layer-average atmospheric temperature time series. *J. Geophys. Res.* **105,** 7337–7356 (2000).
64. Tamura, T., Ohshima, K. I. & Nihashi, S. Mapping of sea ice production for Antarctic coastal polynyas. *Geophys. Res. Lett.* **35,** L07606 (2008).
65. Ohshima, K. I. *et al.* Antarctic Bottom Water production by intense sea-ice formation in the Cape Darnley polynya. *Nat. Geosci.* **6,** 235–240 (2013).
66. Comiso, J. C., Kwok, R., Martin, S. & Gordon, A. L. Variability and trends in sea ice extent and ice production in the Ross Sea. *J. Geophys. Res.* **116,** C04021 (2011).
67. Martin, S., Drucker, R. S. & Kwok, R. The areas and ice production of the western and central Ross Sea polynyas, 1992-2002, and their relation to the B-15 and C-19 iceberg events of 2000 and 2002. *J. Mar. Syst.* **68,** 201–214 (2007).
68. Assmann, K. M. & Timmermann, R. Variability of dense water formation in the Ross Sea. *Ocean Dyn.* **55,** 68–87 (2005).
69. Timmermann, R., Beckmann, A. & Hellmer, H. H. The role of sea ice in the fresh-water budget of the Weddell Sea, Antarctica. *Ann. Glaciol.* **33,** 419–424 (2001).
70. Harms, S., Fahrbach, E. & Strass, V. H. Sea ice transports in the Weddell Sea. *J. Geophys. Res.* **106,** 9057–9073 (2001).
71. Kottmeier, C. & Sellmann, L. Atmospheric and oceanic forcing of Weddell Sea ice motion. *J. Geophys. Res.* **101,** 20809–20824 (1996).
72. Ingleby, B. & Huddleston, M. Quality control of ocean temperature and salinity profiles — Historical and real-time data. *J. Mar. Syst.* **65,** 158–175 (2007).
73. Ren, L., Speer, K. & Chassignet, E. P. The mixed layer salinity budget and sea ice in the Southern Ocean. *J. Geophys. Res.* **116,** C08031 (2011).
74. Jacobs, S. S. Bottom water production and its links with the thermohaline circulation. *Antarct. Sci.* **16,** 427–437 (2004).
75. Depoorter, M. A. *et al.* Calving fluxes and basal melt rates of Antarctic ice shelves. *Nature* **502,** 89–92 (2013).
76. Silva, T. A. M., Bigg, G. R. & Nicholls, K. W. Contribution of giant icebergs to the Southern Ocean freshwater flux. *J. Geophys. Res.* **111,** C03004 (2006).
77. Jacobs, S. S., Fairbanks, R. G. & Horibe, Y. in *Oceanology of the Antarctic Continental Shelf* (ed. Jacobs, S. S.) 59–85 (American Geophysical Union, 1985).
78. Meredith, M. P. *et al.* Changes in the freshwater composition of the upper ocean west of the Antarctic Peninsula during the first decade of the 21st century. *Prog. Oceanogr.* **87,** 127–143 (2010).
79. Orsi, A. H., Whitworth, T. & Nowlin, W. D. On the meridional extent and fronts of the Antarctic Circumpolar Current. *Deep. Res. I* **42,** 641–673 (1995).
80. England, M. H., Godfrey, J. S., Hirst, A. C. & Tomczak, M. The mechanism for Antarctic Intermediate Water renewal in a world ocean model. *J. Phys. Oceanogr.* **23,** 1553–1560 (1993).
81. Talley, L. D. in *The South Atlantic: Present and Past Circulation* (eds Wefer, G. *et al.*) 219–238 (Springer, 1996).
82. Iudicone, D., Rodgers, K. B., Schopp, R. & Madec, G. An exchange window for the injection of Antarctic Intermediate Water into the South Pacific. *J. Phys. Oceanogr.* **37,** 31–49 (2007).
83. Sloyan, B. M. & Rintoul, S. R. Circulation, renewal, and modification of Antarctic Mode and Intermediate Water. *J. Phys. Oceanogr.* **31,** 1005–1030 (2001).
84. Hartin, C. A. *et al.* Formation rates of Subantarctic mode water and Antarctic intermediate water within the South Pacific. *Deep. Res. I* **58,** 524–534 (2011).
85. Durack, P. J. & Wijffels, S. E. Fifty-year trends in global ocean salinities and their relationship to broad-scale warming. *J. Clim.* **23,** 4342–4362 (2010).

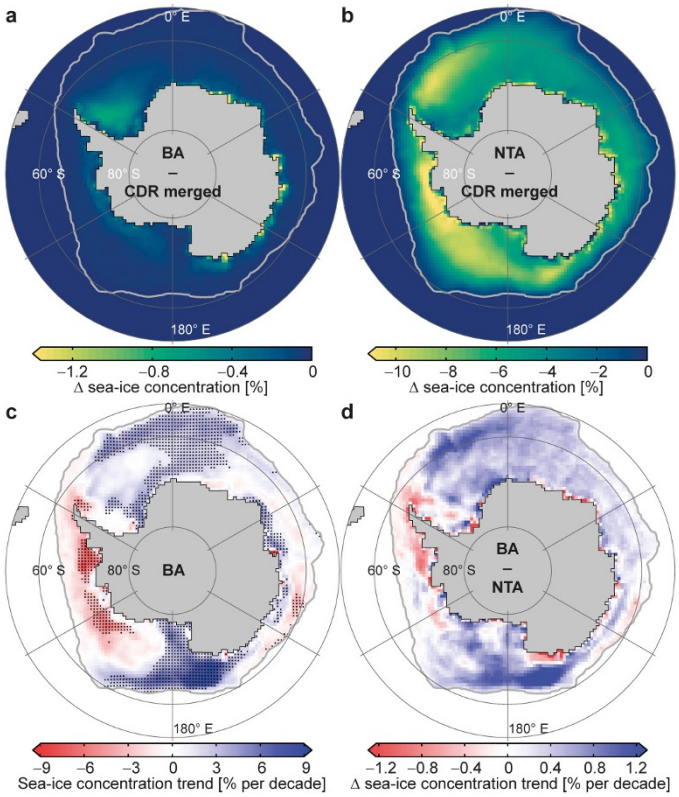

Extended Data Figure 1 | Uncertainties and trends in Antarctic sea-ice concentration over the period 1982–2008. a, BA minus CDR merged data. **b**, NTA minus CDR merged data. **c**, Decadal trends of the BA sea-ice concentration. Stippled trends are statistically significant (at a 90% confidence level or higher using Student's *t*-test). **d**, Decadal trends of the BA minus NTA data. The thick grey line marks the mean sea-ice edge (1% sea-ice concentration). See Methods for details.

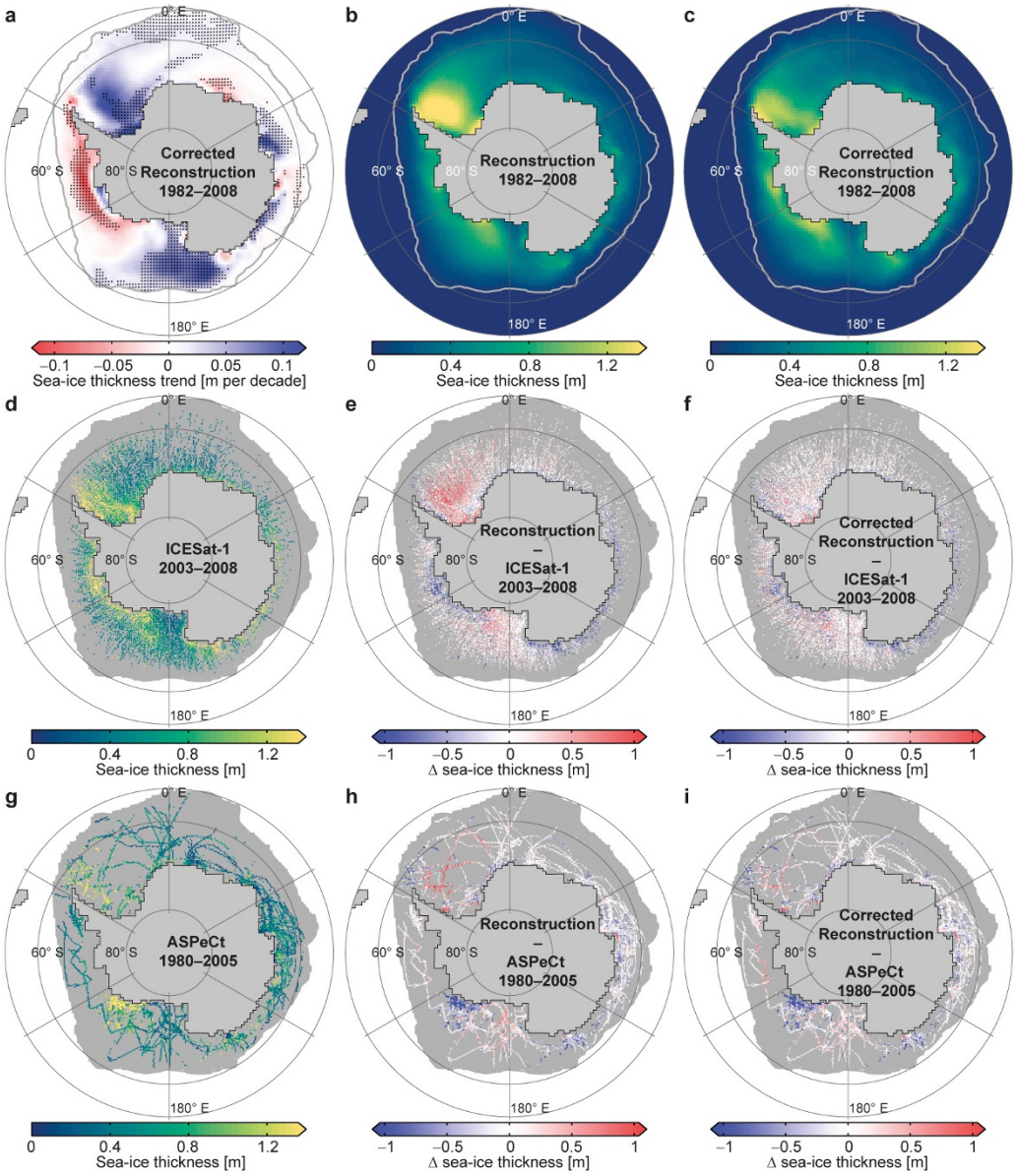

Extended Data Figure 2 | Mean, trend and uncertainty of the Antarctic sea-ice thickness. **a**, Decadal trends of the corrected reconstruction (1982–2008). Stippled trends are statistically significant (at a 90% confidence level or higher using Student's *t*-test). **b**, Mean of the reconstruction (1982–2008). **c**, Mean of the corrected reconstruction (1982–2008). **d**, Mean of the non-gridded ICESat-1 data (2003–2008, 13 campaigns). **e**, Reconstruction minus non-gridded ICESat-1 data (2003–2008). **f**, Corrected reconstruction minus non-gridded ICESat-1 data (2003–2008). **g**, Mean of the ASPeCt data (1980–2005). **h**, Reconstruction minus ASPeCt data (1980–2005). **i**, Corrected reconstructions minus ASPeCt data (1980–2005). The thick grey line marks the mean sea-ice edge (1% sea-ice concentration). Differences are based on data points when both respective products were available. Data points without data in the sea-ice-covered region are shaded in grey in **d**–**i**. See Methods for details.

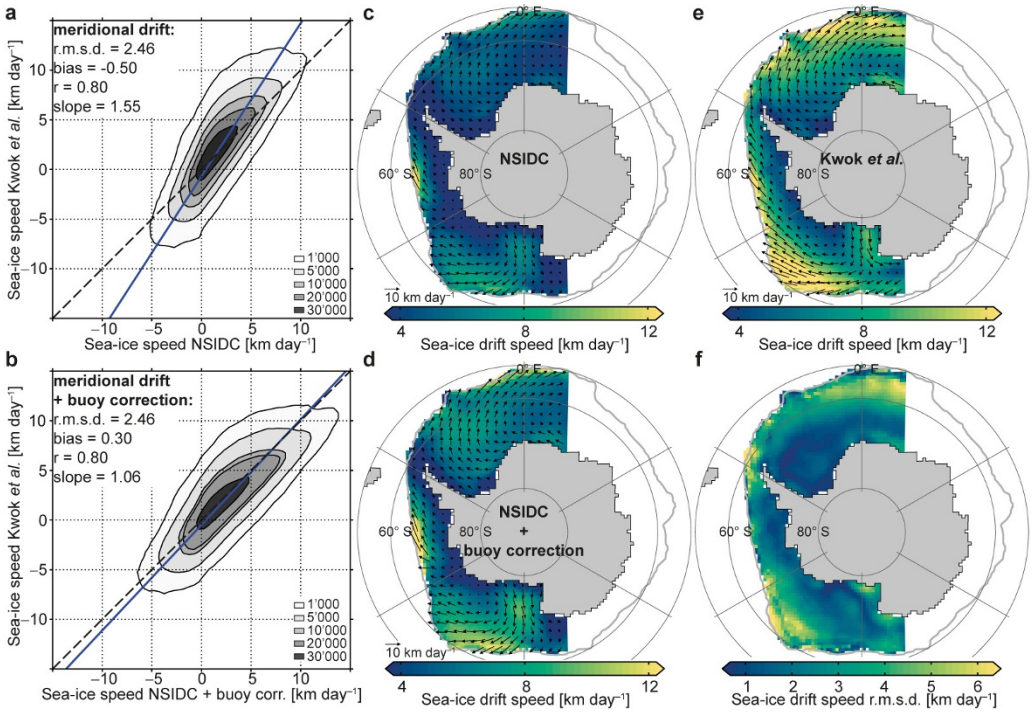

Extended Data Figure 3 | Sea-ice drift speed comparison between the NSIDC and Kwok *et al.* data for the period 1992–2003. a, **b**, Low-pass filtered, 21-d running mean for the original (**a**) and bias-corrected (**b**) daily meridional NSIDC sea-ice drift speed compared with the low-pass filtered daily meridional Kwok *et al.* data. Contours mark the number of grid boxes and the blue line marks the fitted least squares linear regression line. **c**–**e**, Mean sea-ice drift speed of the original (**c**) and bias-corrected NSIDC (**d**) and Kwok *et al.* (**e**) sea-ice drift speed. The arrows denote the drift vectors. **f**, R.m.s. differences between the annual mean bias-corrected NSIDC and Kwok *et al.* sea-ice drift speed. The thick grey line in **c**–**f** marks the mean sea-ice edge (1% sea-ice concentration). Data points were compared when both data sets were available. See Methods for details.

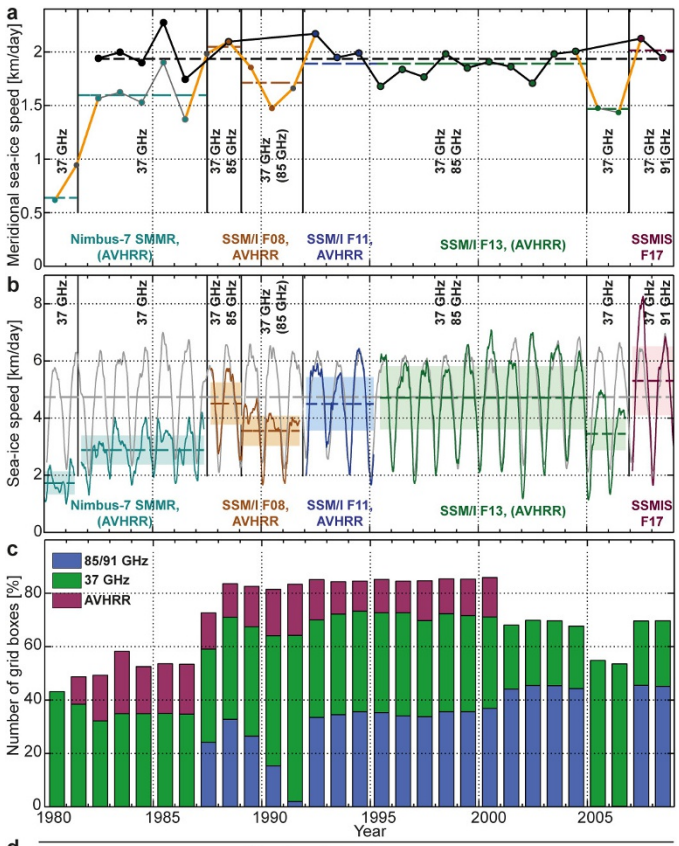

d

Instruments	Passive microwave sensor channels	Start date	End date
Nimbus-7 SMMR	37 GHz	01.01.1980	23.07.1981
Nimbus-7 SMMR, AVHRR	37 GHz	24.07.1981	08.07.1987
SSM/I F08, AVHRR	37 GHz, 85 GHz	09.07.1987	31.01.1989
SSM/I F08, AVHRR	37 GHz, 85 GHz degrading	01.02.1989	02.12.1991
SSM/I F11, AVHRR	37 GHz, 85 GHz	03.12.1991	02.05.1995
SSM/I F13, AVHRR	37 GHz, 85 GHz	03.05.1995	30.12.2000
SSM/I F13	37 GHz, 85 GHz	31.12.2000	31.12.2004
SSM/I F13	37 GHz	01.01.2005	13.12.2006
SSMIS F17	37 GHz, 91 GHz	14.12.2006	31.12.2008

Extended Data Figure 4 | Temporal inhomogeneities in the NSIDC satellite sea-ice drift data. a, Annual mean meridional sea-ice drift speed averaged over the entire sea-ice area (sea-ice concentration >50%). The thick orange lines show the spurious trends due to changes in the underlying data. The black lines shown the data corrected for inconsistencies and used in this study (1982–2008). **b**, Low-pass filtered (91 d running mean) sea-ice drift speed averaged over the entire sea-ice area (sea-ice concentration >50%). The grey lines show the reduced wind speed from ERA-Interim using a reduction factor from the period 1988–2008. The uncorrected data for each satellite instrument combination are shown in colour (dashed lines show the mean over the respective period). The black vertical lines show the periods of the channels. The coloured text denotes the sensors and the frequency of the microwave radiometer channels used. **c**, The fraction of sea-ice covered grid boxes with at least one drift vector observation in a 21-d window and a 75 km × 75 km grid box using the non-gridded NSIDC drift data. The colours indicate the contribution of each sensor and channel. **d**, Different combinations of instruments and passive microwave sensor channels and the related periods underlying the NSIDC sea-ice drift data. See Methods for details.

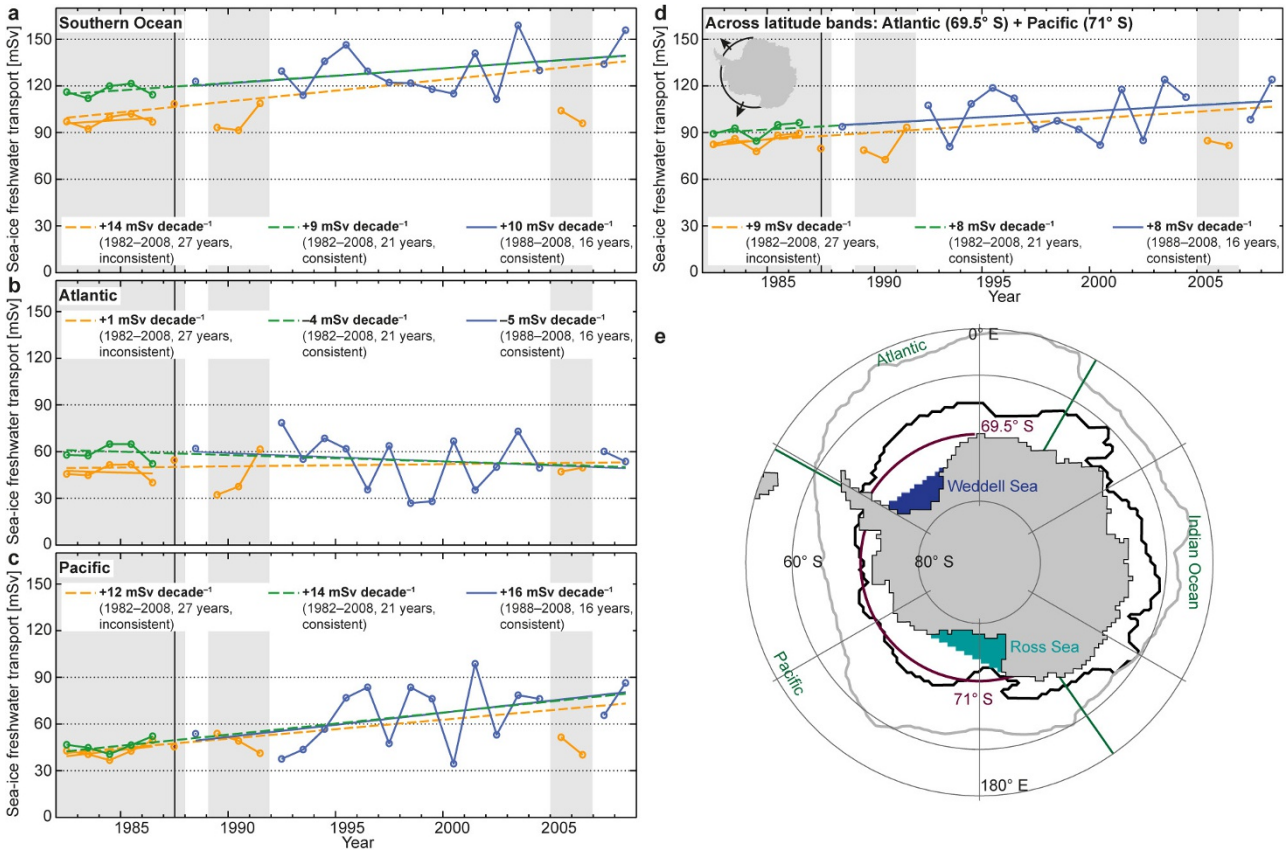

Extended Data Figure 5 | Time series and regions of annual northward sea-ice freshwater transport. a–**c**, Transport from the coastal ocean to the open ocean region in the Southern Ocean (**a**), Atlantic sector (**b**) and Pacific sector (**c**). **d**, Transport across latitude bands in the Atlantic (69.5° S) and Pacific (71° S) sectors. Orange indicates transport estimates if temporal inhomogeneities were not accounted for. Blue shows homogeneous years only. Green represents homogenized time series. Years that have been corrected or removed are shaded in grey. Straight lines show the linear regressions for the periods 1982–2008 (dashed orange and green), 1982–1986 (solid orange) and 1988–2008 (homogeneous years only; solid blue). See Methods for details. **e**, Regions used for the evaluation of the sea-ice freshwater fluxes. Turquoise shading indicates the area south of the coastal Ross Sea flux gate[13,36,66]. Dark blue shading highlights the area south of the coastal Weddell Sea flux gate[13]. Purple lines are the 69.5° S latitude band in the Atlantic sector and the 71° S latitude band in the Pacific sector. The black line shows the smoothed mean zero sea-ice-ocean freshwater flux line that divides the coastal and open ocean regions (see Methods). The thick grey line shows the mean sea-ice edge (1% sea-ice concentration) and the green lines mark basin boundaries.

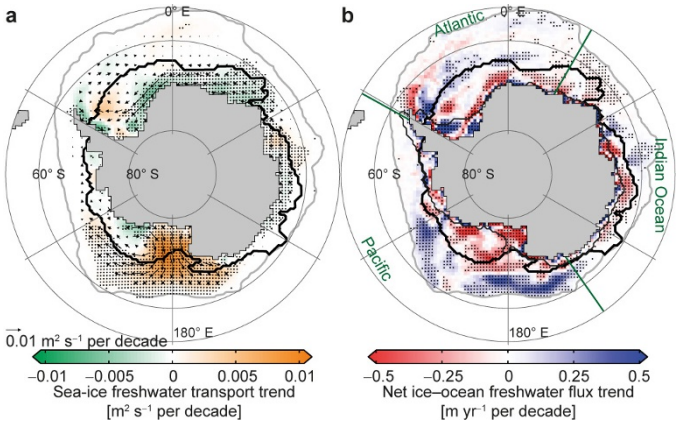

Extended Data Figure 6 | Trends of the net annual freshwater fluxes associated with sea ice over the period 1982–2008 if temporal inhomogeneities in the sea-ice drift data were not considered. **a**, **b**, Linear trends in the meridional sea-ice freshwater transport (**a**) and the net sea-ice–ocean freshwater flux from freezing and melting (**b**). The arrows in **a** denote the trend of the annual transport vectors. Stippled trends are significant at the 90% confidence level using Student's *t*-test (Methods). Thick black lines show the zero sea-ice–ocean freshwater flux line used to divide the coastal from the open ocean regions; the thin black lines mark the continental shelf (1,000 m isobath) the grey lines show the sea-ice edge (1% sea-ice concentration) and the green lines indicate the basin boundaries.

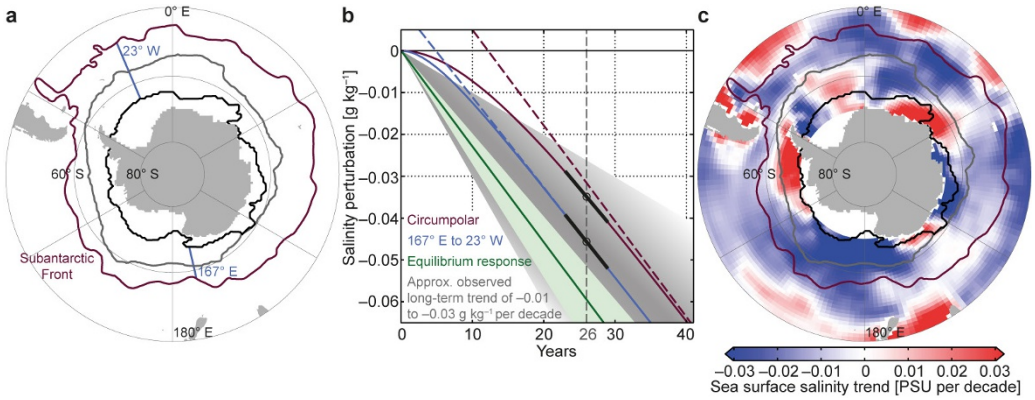

Extended Data Figure 7 | Contribution of sea-ice freshwater flux trends to ocean salinity. a, Map showing the regions used for the estimation of salinity changes due to sea-ice freshwater fluxes. The blue lines show the sector important for AAIW formation (167° E to 23° W). The purple line is the Subantarctic Front[79]. The black line indicates the smoothed mean zero freshwater flux line that divides the coastal and open ocean regions. The thick grey line is the mean sea-ice edge (1% sea-ice concentration). **b**, The salinity response to a freshwater flux perturbation using the long-term equilibrium response (green) and using a delayed response starting in 1982 for a circumpolar reference volume (5×10^6 km^3; purple) or for the region of most AAIW formation (2×10^6 km^3; blue). See Methods for details. Dashed lines show the respective asymptotic equilibrium response. The black lines are the respective current trends. The grey shading shows the approximate observed long-term trend in the AAIW[1,3,4]. **c**, Observed long-term sea-surface salinity trends (data from ref. 85).

Extended Data Table 1 | Mean and uncertainties of the annual sea-ice freshwater fluxes over the period 1982–2008

	Flux [mSv]	Δt [mSv]	ΔA [mSv]	Δc [mSv]	Δh [mSv]	Δu [mSv]	ΔC_{fw} [mSv]
Southern Ocean:							
Transport	+130 ±30	±0	±5	±0	±16	±25	±6
Net open ocean	+130 ±30	±0	±5	±0	±16	±25	±6
Net coastal ocean	-130 ±30	±0	±5	±0	±14	±26	±6
Net continental shelf	-60 ±20	±0	±0	±0	±8	±13	±3
Total melting	+460 ±100	±37	-	±1	±74	±49	±23
Total freezing	−410 ±110	±37	-	±1	±73	±50	±23
Atlantic sector:							
Transport	+60 ±20	±0	±1	±0	±13	±11	±3
Net open ocean	+60 ±20	±0	±1	±0	±13	±11	±3
Net coastal ocean	-50 ±20	±0	±1	±0	±14	±9	±3
Net continental shelf	-20 ±5	±0	±0	±0	±2	±4	±1
Total melting	+180 ±40	±13	-	±0	±25	±21	±9
Total freezing	−160 ±40	±13	-	±0	±25	±19	±9
Indian Ocean sector:							
Transport	+10 ±5	±0	±1	±0	±4	±2	±1
Net open ocean	+10 ±5	±0	±1	±0	±4	±2	±1
Net coastal ocean	-10 ±6	±0	±1	±0	±4	±4	±1
Net continental shelf	-10 ±4	±0	±0	±0	±3	±2	±0
Total melting	+70 ±30	±7	-	±0	±24	±5	±4
Total freezing	−70 ±30	±7	-	±0	±24	±6	±4
Pacific sector:							
Transport	+60 ±20	±0	±2	±0	±9	±12	±3
Net open ocean	+60 ±20	±0	±2	±0	±9	±12	±3
Net coastal ocean	-60 ±20	±0	±2	±0	±9	±13	±3
Net continental shelf	-30 ±9	±0	±0	±0	±6	±6	±2
Total melting	+200 ±50	±17	-	±0	±43	±23	±10
Total freezing	−180 ±60	±17	-	±0	±43	±24	±10

Positive numbers indicate a freshwater flux into the ocean or northward transport ($1\ mSv = 10^3\ m^3\ s^{-1}$). The final uncertainty estimate (95% confidence level) stems from the uncertainties in the filtering of high-frequency temporal noise (Δt), variations of the zero freshwater flux line (ΔA), sea-ice concentration (Δc), sea-ice thickness (Δh), sea-ice drift (Δu) and the freshwater conversion factor (ΔC_{fw}), respectively. See Methods for details. See Fig. 2 for the definition of regions.

Extended Data Table 2 | Decadal trends of the annual sea-ice freshwater fluxes and their uncertainties over the period 1982–2008

	Flux [mSv dec^{-1}]	Δs_e [mSv dec^{-1}]	Δt [mSv dec^{-1}]	ΔA [mSv dec^{-1}]	Δc [mSv dec^{-1}]	Δh [mSv dec^{-1}]	Δu [mSv dec^{-1}]	ΔC_{fw} [mSv dec^{-1}]
Southern Ocean:								
Transport	**+9** ±5	±3.2	±0.3	±1.1	±0.8	±3.0	±1.9	±0.5
Net open ocean	**+10** ±5	±3.5	±0.4	±1.1	±0.8	±3.0	±2.0	±0.5
Net coastal ocean	**-10** ±5	±3.5	±0.2	±1.1	±0.7	±3.3	±1.1	±0.5
Net continental shelf	**-3** ±2	±1.8	±0.0	±0.0	±0.1	±0.8	±0.1	±0.1
Atlantic sector:								
Transport	-4 ±5	±4.3	±0.1	±0.7	±0.1	±1.4	±0.7	±0.2
Net open ocean	-4 ±5	±4.4	±0.1	±0.7	±0.1	±1.4	±0.7	±0.2
Net coastal ocean	+6 ±6	±5.7	±0.1	±0.7	±0.0	±0.6	±1.8	±0.3
Net continental shelf	**+6** ±3	±2.5	±0.0	±0.0	±0.0	±0.6	±1.6	±0.3
Indian Ocean sector:								
Transport	-1 ±1	±1.3	±0.0	±0.2	±0.1	±0.3	±0.2	±0.0
Net open ocean	-1 ±1	±1.3	±0.0	±0.2	±0.1	±0.3	±0.2	±0.0
Net coastal ocean	**-3** ±2	±0.9	±0.0	±0.2	±0.1	±1.1	±0.7	±0.1
Net continental shelf	**+2** ±1	±0.9	±0.1	±0.0	±0.1	±0.3	±0.4	±0.1
Pacific sector:								
Transport	**+14** ±5	±3.4	±0.2	±0.6	±0.7	±1.3	±2.8	±0.7
Net open ocean	**+14** ±5	±3.4	±0.3	±0.5	±0.7	±1.2	±2.9	±0.7
Net coastal ocean	**-13** ±5	±3.6	±0.2	±0.5	±0.6	±1.9	±2.3	±0.7
Net continental shelf	**-10** ±3	±2.6	±0.1	±0.0	±0.2	±1.2	±1.8	±0.5

Positive numbers indicate a freshwater flux trend into the ocean or a northward transport trend (1 mSv per decade = 10^3 m^3 s^{-1} per decade). The final uncertainty estimate (95% confidence level) stems from the standard error of the slope of the regression line (Δs_e), filtering of high-frequency temporal noise (Δt), variations of the zero freshwater flux line (ΔA), sea-ice concentration (Δc), sea-ice thickness (Δh), sea-ice drift (Δu) and the freshwater conversion factor (ΔC_{fw}), respectively. Bold numbers indicate a significance of at least 90% confidence using Student's *t*-test. See Methods for details. See Fig. 2 for the definition of the regions.

Extended Data Table 3 | Sensitivity of the northward sea-ice freshwater transport trend to time periods and homogenization

	Southern Ocean	Atlantic sector	Indian Ocean sector	Pacific sector
1992 – 2004: Flux trend [mSv dec^{-1}]	+4 ±9	-12 ±11	**-5** ±3	**+21** ±10
1992 – 2008: Flux trend [mSv dec^{-1}]	**+11** ±8	-5 ±9	-2 ±2	**+17** ±8
1982 – 2004: Flux trend [mSv dec^{-1}]	**+8** ±5	-6 ±5	-1 ±1	**+15** ±6
1982 – 2008: Flux trend [mSv dec^{-1}]	**+9** ±5	-4 ±5	-1 ±1	**+14** ±5
1982 – 2008 Monte Carlo analysis:				
Flux offset before 1987 [mSv]	+19 ±5	+13 ±7	+3 ±2	+4 ±5
Probability for trend of same sign [%]	100	92	78	100
Probability for significant trend of same sign [%]	92	26	9	100
Posterior trend uncertainty [mSv dec^{-1}]	±5	±6	±2	±5

Positive numbers indicate a northward freshwater transport trend (1 mSv per decade = 10^3 m^3 s^{-1} per decade). Bold numbers indicate a significance of the trend of at least 90% confidence using Student's *t*-test. The Monte Carlo analysis is performed for 10,000 normally distributed sample offsets. Uncertainties (at the 95% confidence level) stem from the standard error of the slope of the regression line and the data uncertainty. See Methods for details. See Fig. 2 for the definition of the regions.